AGU100 ADVANCING EARTH AND SPACE SCIENCE

JGR

Journal of Geophysical Research: Oceans

RESEARCH ARTICLE

10.1029/2018JC013930

Key Points:

- A new modeling methodology to resolve free surface waves and sediment transport with an Eulerian two-phase flow approach is presented
- The effects of progressive wave streaming on bottom boundary layer and sediment transport are isolated by model experiments
- Enhanced onshore sediment transport under surface waves associated with progressive wave streaming is due to a wave-stirring mechanism

Correspondence to:
Y. Kim,
ykim@udel.edu

Citation:
Kim, Y., Cheng, Z., Hsu, T.-J., & Chauchat, J. (2018). A numerical study of sheet flow under monochromatic nonbreaking waves using a free surface resolving Eulerian two-phase flow model. *Journal of Geophysical Research: Oceans*, *123*, 4693–4719. https://doi.org/10.1029/2018JC013930

Received 22 FEB 2018
Accepted 10 JUN 2018
Accepted article online 20 JUN 2018
Published online 5 JUL 2018

A Numerical Study of Sheet Flow Under Monochromatic Nonbreaking Waves Using a Free Surface Resolving Eulerian Two-Phase Flow Model

Yeulwoo Kim[1], Zhen Cheng[2], Tian-Jian Hsu[1], and Julien Chauchat[3]

[1]Center for Applied Coastal Research, Department of Civil and Environmental Engineering, University of Delaware, Newark, DE, USA, [2]Applied Ocean Physics and Engineering, Woods Hole Oceanographic Institution, Woods hole, MA, USA, [3]Université Grenoble Alpes, CNRS, Grenoble INP, LEGI, Grenoble, France

Abstract We present a new methodology that is able to concurrently resolve free surface wavefield, bottom boundary layer, and sediment transport processes throughout the entire water column. The new model, called SedWaveFoam, is developed by integrating an Eulerian two-phase model for sediment transport, SedFoam, and a surface wave solver, InterFoam/waves2Foam, in the OpenFOAM framework. SedWaveFoam is validated with a large wave flume data for sheet flow driven by monochromatic nonbreaking waves. To isolate the effect of free surface, SedWaveFoam results are contrasted with one-dimensional-vertical SedFoam results, where the latter represents the oscillating water tunnel condition. Results demonstrate that wave-averaged total sediment fluxes in both models are onshore-directed; however, this onshore transport is significantly enhanced under surface waves. Onshore-directed near-bed sediment flux is driven by a small mean current mainly associated with velocity skewness. More importantly, progressive wave streaming drives onshore transport mostly in suspended load region due to an intrawave sediment flux. Further analysis suggests that the enhanced onshore transport in suspended load is due to a “wave-stirring” mechanism, which signifies a nonlinear interaction between waves, streaming currents, and sediment suspension. We present some preliminary efforts to parameterize the wave-stirring mechanism in intrawave sediment transport formulations.

1. Introduction

Understanding sediment transport driven by surface waves is a crucial step toward improved coastal morphodynamic modeling. It is well established that sediment transport under steady flow or mildly unsteady flow (such as tidal flows) can be directly associated with bed shear stress and/or free-stream velocity. When such a quasi-steady approach is further applied to wave-driven sediment transport, in which the wave period is often of no more than 10 s and settling velocity of sediment is only a few cm/s, discrepancies emerge (for a comprehensive review, see Van der A et al., 2013). Through a number of oscillating water tunnel (OWT) experiments (e.g., Fredsøe et al., 2003; Jensen et al., 1989; Sumer et al., 2010) and wave-resolving one-dimensional-vertical (1DV) bottom boundary layer models (e.g., Gonzalez-Rodriguez & Madsen, 2007; Holmedal et al., 2003; Ruessink et al., 2009), it has been found that the quasi-steady approach for parameterizing bed shear stress cannot capture the phase lead relative to the flow velocity above the wave bottom boundary layer (WBBL). Such unsteady effect in WBBL may further lead to an underprediction of onshore transport for medium and coarse sand (e.g., Drake & Calantoni, 2001; Hassan & Ribberink, 2010; Hsu & Hanes, 2004; Nielsen, 2006; O’Donoghue & Wright, 2004a, 2004b; Van der A et al., 2013; Watanabe & Sato, 2005). Moreover, due to the so-called phase lag effect, which signifies the unsteadiness between sediment transport rate and bed shear stress, the quasi-steady assumption fails to capture offshore transport for fine sand driven by velocity skewed waves (Dohmen-Janssen et al., 2002; O’Donoghue & Wright, 2004a, 2004b).

While a significant progress has been made in understanding wave-driven sediment transport based on OWT data and 1DV bottom boundary layer models, main differences exist between these idealized apparatus/domains and realistic WBBL under surface waves. The oscillatory bottom boundary layer generated in OWT is only approximately similar to the WBBL under surface waves mainly because of its homogeneous flow field in the direction of wave propagation. Considering a small amplitude (linear) progressive surface wave train, a slight inhomogeneity exists in the direction of wave propagation, which results in an onshore-directed streaming current in the wave-averaged formulation (Longuet-Higgins, 1953). In this paper, we will follow the study of Kranenburg et al. (2012) and call this onshore-directed streaming current as the progressive wave streaming. On the other hand, under waves with high-velocity skewness, turbulence under wave crest is larger than that during wave trough, which results in an offshore-directed streaming current, called waveshape streaming (Kranenburg et al., 2012; Ribberink & Al-Salem, 1994; Trowbridge & Madsen, 1984). For realistic surface waves in shallow water, both streaming processes coexist along with the unsteady effect. These different mechanisms counteract one with another and determine the net sediment transport. In the past decade, several sheet flow experiments driven by nonbreaking, highly nonlinear waves were carried out in large wave flumes (e.g., Dohmen-Janssen & Hanes, 2002, 2005; Ribberink et al., 2000; Schretlen, 2012). For example, a noteworthy increment in wave-averaged (net) onshore sediment transport rate was observed in Dohmen-Janssen and Hanes (2002, see their Figure 5) when compared the results with OWT data under similar wave intensity and grain properties.

Similarly, the boundary layer approximation has been routinely used for numerical models to study wave-driven sediment transport, which mimics OWT condition. In the so-called 1DV formulation, the streamwise flow development is neglected and free-stream velocity measured some distance above the bottom boundary layer is converted to a prescribed horizontal pressure gradient to drive the numerical model. When driving the model with a skewed velocity time series, the waveshape streaming effect is captured; however, the effect of progressive wave streaming is missing. To approximately capture the effect of boundary layer inhomogeneity, the horizontal velocity gradient can be transformed into time derivatives following $\partial u/\partial x = -1/c\partial u/\partial t$, in which c is the wave celerity. This approximation is justified by assuming small-amplitude waves (Trowbridge & Madsen, 1984; small ak, in which a is the wave amplitude and k is the wave number). This approximation has been adopted in 1DV single-phase WBBL model for sediment transport to study sandbar migration (Henderson et al., 2004) and to understand the relative importance of progressive wave streaming and waveshape streaming on sand transport (Kranenburg et al., 2012; Kranenburg et al., 2013). However, its applicability to nonlinear waves, which often come with rapid change of waveshape, is unclear.

In the past two decades, a range of 1DV two-phase sediment transport models have been developed to study the sheet flows in the WBBL (e.g., Amoudry et al., 2008; Cheng et al., 2017; Dong & Zhang, 1999; Hsu et al., 2004). These two-phase models do not require conventional bedload/suspended load assumptions as were used in the single-phase models. These two-phase models have brought valuable insights on practical parameterizations of pickup flux and bed shear stress (Amoudry & Liu, 2010; Yu et al., 2010) as well as improving the physical understanding of sheet flows (e.g., Dong & Zhang, 1999; Li et al., 2008). More recently, the spatial/temporal derivative transformation discussed previously was applied to these two-phase models to study the effect of progressive wave streaming on sheet flows (Kranenburg et al., 2014; Yu et al., 2010). To understand the various mechanisms associated with free surface waves, unsteadiness in WBBL, and the resulting sediment transport, there is a need to develop a new numerical modeling framework based on two-phase flow formulation that is able to concurrently simulate free surface wave propagation, WBBL, and fine-scale sediment transport processes.

Motivated by this need, a free surface resolving Eulerian two-phase sediment transport model is developed in this study by merging two existing numerical models, SedFoam (Chauchat et al., 2017; Cheng et al., 2017), InterFoam (Berberović et al., 2009; Klostermann et al., 2013), and waves2Foam (Jacobsen et al., 2012) in the OpenFOAM framework. SedFoam can resolve the full vertical profile of sediment transport using the Reynolds-averaged Eulerian two-phase flow equations with closures of intergranular stresses and a k-ε turbulence model (Cheng et al., 2017). It has been validated with measured data for several sheet flow conditions in OWT reported by O'Donoghue and Wright (2004a). On the other hand, InterFoam is capable of solving the flow characteristics between two immiscible fluids (i.e., air and water), in line with the well-known volume-of-fluid method (Hirt & Nichols, 1981). InterFoam simplifies air and water phases as a mixture and tracks the air-water interface with the volumetric concentration of the water phase using an interface compression method (Klostermann et al., 2013) while limiting the numerical diffusion at the interface. It has been proven that InterFoam can be applied in energetic flow conditions such as a dam-break-driven swash (e.g., Briganti et al., 2016; Kim et al., 2017). A comprehensive wave toolbox for InterFoam, called waves2Foam (Jacobsen et al., 2012), which has been widely adopted to explore various wave-induced processes in surf zone (e.g., Jacobsen et al., 2014; Zhou et al., 2017), is also incorporated to generate and absorb surface waves. Since all these solvers and toolbox are based on the framework of open-source CFD library, OpenFOAM, adding the capabilities into a new solver is made a lot easier.

The purpose of this study is to present such new numerical modeling strategy. To demonstrate the model capability, it is first applied to simulate sheet flow driven by nonbreaking monochromatic waves in a large wave flume reported by Ribberink et al. (2000) and Dohmen-Janssen and Hanes (2002). Model formulations and numerical implementations are discussed in section 2. Section 3 presents the main model results including model validation and several important sheet flow characteristics in WBBL under waves. Section 4 is discussions on parameterizing wave-driven sediment transport. Finally, the main conclusions of this study are summarized in section 5.

2. Model Formulations

2.1. Governing Equations

As a first step in the model development, we adopt a Reynold-averaged approach to avoid resolving 3-D turbulence with a wide range of scales. In modeling sediment transport under surface waves, three phases (i.e., air, water, and dispersed sediment) are involved. The Reynolds-averaged mass conservation equations for air, water, and sediment phases can be written as (e.g., Berberović et al., 2009; Drew, 1983)

$$\frac{\partial \phi^a}{\partial t} + \frac{\partial \phi^a u_i^a}{\partial x_i} = 0, \tag{1}$$

$$\frac{\partial \phi^w}{\partial t} + \frac{\partial \phi^w u_i^w}{\partial x_i} = 0, \tag{2}$$

$$\frac{\partial \phi^s}{\partial t} + \frac{\partial \phi^s u_i^s}{\partial x_i} = 0. \tag{3}$$

The variable ϕ^k represents the volumetric concentration where superscript "k" stands for "a" for air, "w" for water, and "s" for sediment phases, respectively. The global mass conservation imposes $\phi^a + \phi^w + \phi^s = 1$. The variable u^k represents the velocity of each phase. In this study, the air and water (fluid) phases are modeled as two immiscible fluids with their interface resolved numerically by an interface tracking scheme (see section 2.3). On the other hand, the (solid) sediment phase is modeled as a miscible phase in the fluids. Therefore, equations (1) and (2) for mass conservation of air and water can be combined as the fluid phase:

$$\frac{\partial \phi^f}{\partial t} + \frac{\partial \phi^f u_i^f}{\partial x_i} = 0, \tag{4}$$

where superscript "f" represents the mixture of air and water (fluid) phases with $\phi^a + \phi^w = \phi^f$ and $u^f = (u^a\phi^a + u^w\phi^w)/\phi^f$, while the mass conservation of sediment phase is governed by equation (3). Hence, three phases involved here are simplified into two (miscible) phases and the term "two-phase" will be used to refer to the air-water mixture (fluid) and sediment (solid) phases throughout the paper. The Reynolds-averaged momentum equations for the air-water mixture and sediment phases can be written as (e.g., Drew, 1983)

$$\frac{\partial \rho^f \phi^f u_i^f}{\partial t} + \frac{\partial \rho^f \phi^f u_i^f u_j^f}{\partial x_j} = -\phi^f \frac{\partial p^f}{\partial x_i} + \rho^f \phi^f g \delta_{i3} - \sigma_t \gamma \frac{\partial \phi^a}{\partial x_i} + \frac{\partial \tau_{ij}^f}{\partial x_j} + M_i^{fs}, \tag{5}$$

$$\frac{\partial \rho^s \phi^s u_i^s}{\partial t} + \frac{\partial \rho^s \phi^s u_i^s u_j^s}{\partial x_j} = -\phi^s \frac{\partial p^f}{\partial x_i} - \frac{\partial p^s}{\partial x_i} + \rho^s \phi^s g \delta_{i3} + \frac{\partial \tau_{ij}^s}{\partial x_j} + M_i^{sf}, \tag{6}$$

where ρ^s = 2,650 kg/m^3 is the sediment density and ρ^f is the mixture fluid density, satisfying $\rho^f = (\rho^a\phi^a + \rho^w\phi^w)/\phi^f$. Here we specify ρ^a = 1 kg/m^3 and ρ^w = 1,000 kg/m^3. The variable p^f is the fluid pressure; $g = -9.8$ m^2/s is the gravitational acceleration. The third term on the right-hand-side (RHS) of equation (5) represents surface tension where σ_t is the surface tension coefficient (we specify σ_t = 0.0074 kg/s^2 for the air-water interface at 20°C) and γ is the surface curvature. The fluid stress, τ_{ij}^f, is the sum of grain-scale viscous stress and turbulent Reynolds stress with the latter calculated by a two-equation k-ε turbulence model (see section 2.2.2) for two-phase flow. The particle pressure, p^s, and particle shear stress, τ_{ij}^s, are modeled with the kinetic theory of granular flow for particle collision at low to moderate concentration and phenomenological closures for enduring contact at high sediment concentration (see section 2.2.3).

Table 1
List of Coefficients for Fluid Turbulence Closure

C_μ	$C_{1\varepsilon}$	$C_{2\varepsilon}$	$C_{3\varepsilon}$	$C_{4\varepsilon}$	σ_c	σ_ε	B
0.09	1.44	1.92	1.2	1.0	1.0	1.3	0.16

2.2. Closures

2.2.1. Interphase Momentum Exchange

The interphase momentum transfer between the carrier flow (i.e., mixture of air and water) and sediment phases follows Newton's third law, $M_i^{fs} = -M_i^{sf}$. Following Cheng et al. (2017), it consists of drag force due to Reynolds-averaged mean velocity difference and turbulent suspension modeled with a gradient transport formulation:

$$M_i^{fs} = -\phi^s\beta\left(u_i^f - u_i^s\right) + \beta\frac{\nu^{ft}}{\sigma_c}\frac{\partial\phi^s}{\partial x_i}, \tag{7}$$

where β is the drag parameter following Ding and Gidaspow (1990), ν^{ft} is the fluid turbulent viscosity (see section 2.2.2), and σ_c is the Schmidt number (see Table 1). More detailed formulation is referred to Cheng et al. (2017).

2.2.2. Fluid Turbulence Closures

Fluid stresses, τ_{ij}^f, in equation (5) include turbulent Reynolds stress, R_{ij}^{ft}, and grain-scale components, r_{ij}^f. The Reynolds stress represents the effect of turbulent fluctuations larger than grain scale, and the grain-scale stress consists of small-scale viscous stress and fluid-particle interactions. Consistent with Cheng et al. (2017), only the viscous stress is considered for grain-scale component, and the total fluid stress can be written as

$$\tau_{ij}^f = R_{ij}^{ft} + r_{ij}^f = \rho^f\phi^f\left[2\left(\nu^{ft} + \nu^f\right)S_{ij}^f - \frac{2}{3}k^f\delta_{ij}\right], \tag{8}$$

in which the kinematic viscosity of carrier fluid, ν^f, is defined as $\nu^f = (\rho^a\phi^a\nu^a + \rho^w\phi^w\nu^w)/(\rho^a\phi^a + \rho^w\phi^w)$ where $\nu^a = 1.48\times10^{-5}$ m^2/s and $\nu^w = 10^{-6}$ m^2/s. The turbulent eddy viscosity, ν^{ft}, is calculated by turbulent kinetic energy (TKE), k^f, and turbulent dissipation rate ε^f as $\nu^{ft} = C_\mu(k^f)^2/\varepsilon^f$ where C_μ is an empirical coefficient (Table 1). The deviatoric part of the fluid phase strain rate, S_{ij}^f, is defined as $S_{ij}^f = \frac{1}{2}\left(\frac{\partial u_i^f}{\partial x_j} + \frac{\partial u_j^f}{\partial x_i}\right) - \frac{1}{3}\frac{\partial u_k^f}{\partial x_k}\delta_{ij}$.

The TKE equation is modified from standard k^f equation to incorporate additional turbulence induced by sediment in water. Compared to previous two-phase sediment transport models (Cheng et al., 2017; Yu et al., 2010), excessive diffusion occurring at the air-water interface can also be controlled here by considering the sharp density gradient (Zhang et al., 2015). Hence, the density gradient is also combined with the following balance equation for TKE as

$$\begin{aligned}\frac{\partial\rho^f k^f}{\partial t} + \frac{\partial\rho^f u_j^f k^f}{\partial x_j} = R_{ij}^{ft}\frac{\partial u_i^f}{\partial x_j} + \frac{\partial}{\partial x_j}\left[\rho^f\left(\nu^f + \frac{\nu^{ft}}{\sigma_k}\right)\frac{\partial k^f}{\partial x_j}\right] \\ - \rho^f\varepsilon^f - \frac{2\beta(1-\alpha)\phi^s k^f}{\phi^f} - \frac{\rho^f\nu^{ft}}{\phi^f\sigma_c}\frac{\partial\phi^s}{\partial x_j}(s-1)g\delta_{j3},\end{aligned} \tag{9}$$

where $\sigma_k = 1$ is the empirical TKE Schmidt number (e.g., Rodi, 1993) and $s = \rho^s/\rho^f$ is the specific density of the sediment. The fourth term on the RHS of equation (9) indicates the TKE attenuation due to particle inertial effect. Specifically, the parameter $\alpha = e^{-BS_t}$ parameterizes the level of correlation between fluid and sediment velocity fluctuations (Chen & Wood, 1985; Danon et al., 1977) in which B is an empirical coefficient (see Table 1) and $S_t = t_p/t_l$ is the Stokes number quantified by particle response time, $t_p = \rho^s/\beta$, and characteristic time scale of energetic eddies, $t_l = k^f/(6\varepsilon^f)$ (Balachandar & Eaton, 2009). The last term in equation (9) is the buoyancy effect that can attenuate turbulence due to stable density stratification.

The balance equation for turbulence dissipation rate is written as

$$\begin{aligned}\frac{\partial\rho^f\varepsilon^f}{\partial t} + \frac{\partial\rho^f u_j^f\varepsilon^f}{\partial x_j} = C_{1\varepsilon}R_{ij}^{ft}\frac{\varepsilon^f}{k^f}\frac{\partial u_i^f}{\partial x_j} + \frac{\partial}{\partial x_j}\left[\rho^f\left(\nu^f + \frac{\nu^{ft}}{\sigma_\varepsilon}\right)\frac{\partial\varepsilon^f}{\partial x_j}\right] - C_{2\varepsilon}\rho^f\frac{\varepsilon^f}{k^f}\varepsilon^f \\ - C_{3\varepsilon}\frac{\varepsilon^f}{k^f}\frac{2\beta(1-\alpha)\phi^s k^f}{\phi^f} - C_{4\varepsilon}\frac{\varepsilon^f}{k^f}\frac{\rho^f\nu^{ft}}{\phi^f\sigma_c}\frac{\partial\phi^s}{\partial x_j}(s-1)g\delta_{j3},\end{aligned} \tag{10}$$

where the empirical coefficient $C_{1\varepsilon}$, $C_{2\varepsilon}$, $C_{3\varepsilon}$, $C_{4\varepsilon}$, and σ_ε are summarized in Table 1. Consistent with equation (9), the fourth term in the RHS of equation (10) is a damping term due to particle inertia, and the last term is the buoyancy effect due to the density stratification.

2.2.3. Particle Stress Closures

The particle stresses caused by intergranular interactions consist of intermittent collision and enduring contact/frictional forces (e.g., Hsu et al., 2004). Hence, the particle pressure, p^s, and shear stress, τ_{ij}^s, are expressed as summations of a collisional component (superscript "*sc*") and a frictional contact component (superscript "*sf*"):

$$p^s = p^{sc} + p^{sf}, \tag{11}$$

$$\tau_{ij}^s = \tau_{ij}^{sc} + \tau_{ij}^{sf}. \tag{12}$$

The collisional component of particle pressure, p^{sc}, and particle shear stress, τ^{sc}, are modeled using the concept of granular temperature, Θ, from the kinetic theory of granular flow (Ding & Gidaspow, 1990; Jenkins & Savage, 1983):

$$p^{sc} = \rho^s \phi^s [1 + 2(1+e) g_{s0}]\Theta, \tag{13}$$

$$\tau_{ij}^{sc} = 2\mu^{sc} S_{ij}^s + \lambda \frac{\partial u_k^s}{\partial x_k}\delta_{ij}, \tag{14}$$

where e is the restitution coefficient and g_{s0} is the radial distribution function (Carnahan & Starling, 1969). The granular temperature Θ is calculated by its balance equation that accounts for advection, diffusion, shear production, dissipation to due inelastic collision, and particle-induced fluctuations (Cheng et al., 2017; Ding & Gidaspow, 1990). The particle shear viscosity, μ^{sc}, and bulk viscosity, λ, are functions of granular temperature and calculated by the kinetic theory (Gidaspow, 1994). The deviatoric part of the sediment phase strain rate, S_{ij}^s, is defined as $S_{ij}^s = \frac{1}{2}\left(\frac{\partial u_i^s}{\partial x_j} + \frac{\partial u_j^s}{\partial x_i}\right) - \frac{1}{3}\frac{\partial u_k^s}{\partial x_k}\delta_{ij}$.

When sediment concentration is very high, intermittent collisions become unlikely and the modeled granular temperature diminishes. Particle pressure and shear stress are taken over by the frictional contact component. The particle pressure due to enduring contact, p^{sf}, and particle shear stress due to frictional contact, τ^{sf}, are modeled by phenomenological closure (Cheng et al., 2017; Johnson & Jackson, 1987; Schaeffer, 1987; Srivastava & Sundaresan, 2003):

$$p^{sf} = \begin{cases} 0, & \phi^s < \phi_f^s \\ F\dfrac{\left(\phi^s - \phi_f^s\right)^a}{\left(\phi_{\max}^s - \phi^s\right)^b}, & \phi^s \geq \phi_f^s \end{cases}, \tag{15}$$

$$\tau_{ij}^{sf} = -2\mu^{sf} S_{ij}^s, \tag{16}$$

where $F = 0.05$, $a = 3$, and $b = 5$ are empirical coefficients and we specify the threshold values for $\phi_f^s = 0.57$ and $\phi_{\max}^s = 0.635$. The variable ϕ_f^s indicates the limit where enduring contact becomes dominant. The frictional viscosity, μ^{sf}, is calculated by combining p^{sf} (Johnson & Jackson, 1987) and frictional viscosity (Schaeffer, 1987) following Srivastava and Sundaresan (2003):

$$\mu^{sf} = \frac{\sqrt{2} p^{sf} \sin(\theta_f)}{2\sqrt{S_{ij}^s S_{ij}^s}} \tag{17}$$

where θ_f is the angle of repose, taken to be 28° for sand.

2.3. Numerical Implementations

The standard PIMPLE (i.e., PISO-SIMPLE algorithm) is adopted in this study to solve the momentum equations (equations (6) and (7)). Then intermediate velocities are calculated from the initial condition or previous time step without a pressure correction following a segregated pressure correction method (e.g., Passalacqua & Fox, 2012; Rusche, 2002). Then, the velocities can be calculated by correcting the intermediate velocities with pressure gradients. After solving the pressure, the velocities are updated while satisfying their mass conservation and then the updated velocities are used to update the volumetric concentrations of each phase, turbulence quantities, and stresses.

It should be reiterated here that the continuity and momentum equations for the air-water mixture phase (see equations (4) and (5)) is numerically solved following the air-water interface tracking strategy of InterFoam (Berberović et al., 2009; Klostermann et al., 2013). The equation (4) is converted into

$$\frac{\partial \phi^w}{\partial t} + \frac{\partial \phi^w u_i^f}{\partial x_i} + \frac{\partial \left(\phi^a \phi^w u_i^r / \phi^f \right)}{\partial x_i} = 0, \tag{18}$$

where u_i^r represents a relative velocity between air and water phases, obtained by iterations using the interface compression method while minimizing the diffusion at the air-water interface (Berberović et al., 2009; Klostermann et al., 2013). Then the advection term in equation (5) is also incorporated with the interface compression method to constrain the excessive flux at the air-water interface, expressed as

$$\frac{\partial \rho^f \phi^f u_i^f u_j^f}{\partial x_j} = \frac{\partial \left[\rho^a \phi^f u_j^f + (\rho^w - \rho^a) \phi^w u_j^f \right] u_i^f}{\partial x_j}, \tag{19}$$

where $\phi^w u_i^f$ is obtained from equation (18).

Gauss theorem is applied to convert the convection terms into surface integrals for each cell. Then using a second-order total variation diminishing scheme, sediment fluxes are calculated based on Sweby limiter (Sweby, 1984). The mixture fluxes are calculated using upwind scheme. For the diffusion terms, central difference scheme and nonorthogonal correction (Jasak, 1996) are applied to discretize and evaluate the resulting fluxes.

The implicit second-order backward scheme is adopted for a time integration. The time step of the model satisfies the Courant-Friedrichs-Lewy condition, defined as

$$C_0 = \begin{cases} \dfrac{U^f \Delta t}{\Delta} \le C_{\max}, & U^f > U^s \\ \dfrac{U^s \Delta t}{\Delta} \le C_{\max}, & U^f \le U^s \end{cases}, \tag{20}$$

where C_0 is the courant number, U is the absolute velocity magnitude, Δ is the characteristic length of grid size, and Δt is automatically adjusted time step. To ensure the numerical stability and optimal calculation time, $C_{\max}$ = 0.2 is used.

The newly developed solver, named SedWaveFoam, is designed to simulate sediment transport under surface waves. The remaining of the paper is devoted to demonstrating its capability to simulate sheet flow driven by nonbreaking waves. However, technically, we believe that the model can also be used to simulate sediment transport under breaking waves as long as the air phase does not directly interact with the sediment phase. The direct interaction between the air and sediment phases has not been tested, and this important capability (e.g., applying for swash zone process) will be extended in future study.

3. Results

The SedWaveFoam is validated with the large wave flume sheet flow data under monochromatic nonbreaking waves reported in Ribberink et al. (2000) and Dohmen-Janssen and Hanes (2002). The sheet flow experiment was carried out in the large wave flume (Großer WellenKanal) of the ForschungsZentrum Küste in Hannover, Germany. Großer WellenKanal has a length of 300 m, a width of 5 m, and a depth of 7 m. In the experiment of Dohmen-Janssen and Hanes (2002), the water depth at the wave paddle was 4.25 m. At the downstream end of the wave flume, wave energy was dissipated by a steep beach with a 1/10 slope. The sand bed, which had a length of 45 m and a depth of 0.75 m, was established in the middle of the wave flume (85 m downstream of the wave paddle). Hence, the water depth at the measurement section was reduced to 3.5 m. The sand bed was constructed of well-sorted quartz with a median grain diameter d_{50} of 0.24 mm (d_{10} = 0.173 mm and d_{90} = 0.277 mm). The monochromatic waves with several different wave periods (T) and heights (H) were generated at the wave paddle, which had a shape similar to cnoidal waves.

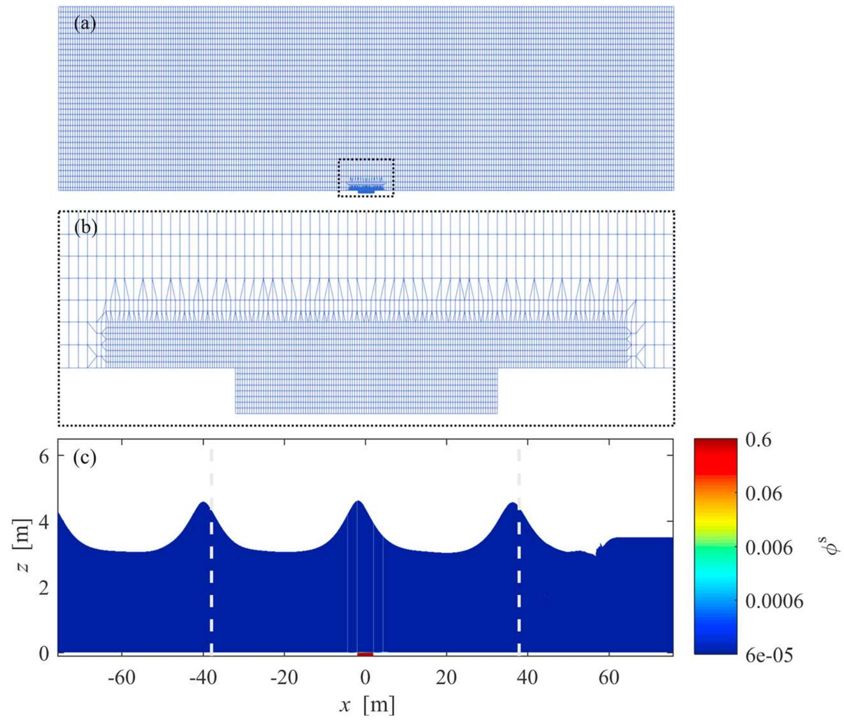

Figure 1. A numerical wave flume with (a) wide view of mesh, (b) enlarged view of mesh near the sediment pit (black dotted square in Figure 1a), and (c) a snapshot at t = 71.1 s with different colors represent air (white), water (blue), and sediment (red) phases (sediment phase around x = 0). For visibility, the mesh is down-sampled and vertical scale is stretched by 7 times. The gray dashed lines in Figure 1c represent the boundaries of relaxation zone.

A multiple transducer array was deployed to survey the bed level change with horizontal and vertical resolutions less than 3 mm. The bed level change was used to estimate net sediment transport rate. Two conductivity concentration meter (CCM) probes were buried under the sand bed to measure sediment concentration in the concentrated region of transport. The CCM probes were deployed with a gap of 15 mm in streamwise direction at the same vertical location to estimate grain velocities. Then, for the repeated runs, the CCM probes were installed at different vertical locations to obtain the profile of sediment concentration in the sheet flow layer. For the suspended sediment, two sets of acoustic backscatter sensors (ABS) were used with a vertical resolution of 7.5 mm. The near-bed velocity of the water phase was measured using an acoustic Doppler velocimeter located at 109 mm above the sand bed.

3.1. Model Setup

Since the flow in the physical experiment is homogeneous in the spanwise direction, a 2-D model domain is adopted. As presented in Figure 1, the x direction is denoted as wave propagation direction with x = 0 defined at the middle of the sediment pit. The vertical z direction is defined as positive upward with z = 0 located at the top of the initial sand bed (initial bed level). We simulate only the flat portion of the wave flume to reduce computational cost; hence, the water depth in the model domain is given as a constant 3.5 m. The numerical model domain is 151.56 m long (about 5 wavelengths, 5 L) and 6.5 m deep. The sediment pit of 4 m long and 0.1 m deep is located at about 2 L downstream from the inlet. Using the d_{50} value reported from the physical experiment, sediment of grain diameter of d = 0.24 mm and specific gravity of 2.65 are specified in the model. It should be noted that the maximum volumetric concentration of sediment phase computed by numerical model is $\phi^s_{\max} = 0.61$, similar to the typical packing limit for uniform and spherical particles. However, this value is smaller than the value of 0.67 reported in the physical experiment (Dohmen-Janssen & Hanes, 2002). The mesh is first constructed with uniform grids of 4.8 cm width and 1.6 cm height (Figure 1a). Then, the grids near the sediment pit (a region of 8 m in length and 0.2 m in height) are refined with five layers of triangular meshes using a tool called snappyHexMesh (Jackson, 2012) such that fine grid size of a width of 1.5 mm and height of 0.52 mm is used to model sheet flow (see Figure 1b). A total number of 2.85 million computational grid points is used for the simulation.

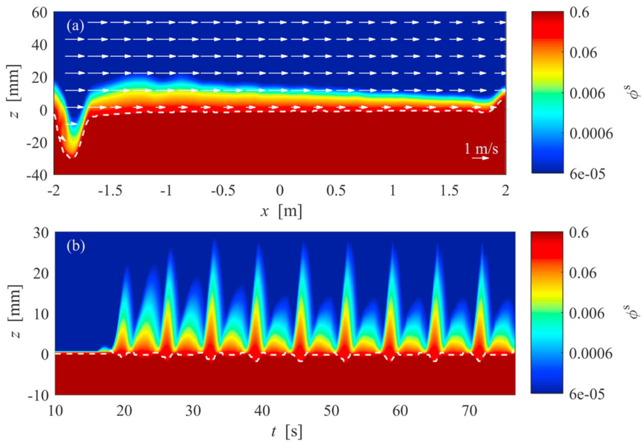

Figure 2. The snapshots of (a) ϕ^s over the entire sediment pit at t = 71.1 s and (b) temporal evolution of ϕ^s at the center of sediment pit (x = 0). The vectors in (a) represent fluid velocity u_i^f, and the white dashed curves in (a) and (b) represent the bed location.

A wall boundary is specified at the bottom with no-flux boundaries for scalar quantities and wall-normal velocity components. The velocity components parallel to the wall are set to no-slip boundary condition. It is noted that in the sediment pit region, this no-slip boundary is of minor importance since it is below a layer of immobile sand bed. The top boundary is specified as atmospheric boundary condition and the two spanwise lateral boundaries are treated as empty condition in OpenFOAM. Using waves2Foam (Jacobsen et al., 2012), a relaxation zone of 1 L is adopted at each end of the wave flume to minimize reflected waves (Figure 1c). According to Dohmen-Janssen and Hanes (2002), the surface wave generated in the wave flume was similar to cnoidal waves. Among the many different wave conditions, the test condition, mh, corresponding to H = 1.6 m and T = 6.5 s at the wave paddle is selected here due to the availability of data. In the numerical model, monochromatic waves having H = 1.55 m and T = 6.5 s are sent into the domain using tenth-order stream function to match the velocity at the top of the WBBL.

The model can produce the expected spatial (Figure 2a) and temporal (Figure 2b) evolutions of sediment concentration in a sheet flow driven by surface waves. Figure 2a shows the x-z plane snapshot (at t = 71.1 s) of the sediment volumetric concentration (ϕ^s) of the entire sediment pit region with the fluid velocity (u_i^f) represented by white vectors (down sampled) and the instantaneous immobile bed location illustrated using the dashed line (see section 3.3 for more details on the definition of immobile bed location). Noticeable scour (>30 mm) is observed at the upstream side of the sediment pit ($x = -2$ m) caused by the absence of sediment flux from the upstream. Likewise, accumulation of sediment is observed at the downstream edge of the sediment pit (x = 2 m). Those morphological features are a signature of a net onshore sediment transport in this configuration. The central region of the sediment pit (around x = 0), however, is demonstrated to be sufficiently far from the two ends of the sediment pit, and a region of flat bed is observed. The slopes of the scour hole were less than the angle of repose, which was specified to be 28° in the model (see equation (17)). By checking the wave-averaged ϕ^s and u^f at different streamwise locations, we confirmed that the region in range of -0.4 m $< x <$ 1.0 m is in quasi-equilibrium (i.e., wave-averaged flow quantities are homogeneous in the streamwise direction and time series of flow quantities at different streamwise location are nearly identical after a temporal shift). The time series of ϕ^s up to the tenth wave at x = 0 is presented in Figure 2b. Sediment concentration evolution among the seventh and the tenth waves are nearly identical and can be considered as in the quasi-steady state. Hence, the model results for the tenth wave (t = 70.2 – 76.7 s) at the center location (x = 0) are selected for model validations and further analysis.

3.2. Model Validations

Reynolds-averaged model results are compared with the measured data. To obtain ensemble-averaged flow quantities approximately in the measured data, wave-phase-average over about 1,000 waves were carried out (Dohmen-Janssen & Hanes, 2002). Normalized root-mean-square error (NRMSE) and index of agreement (Willmott, 1981; Willmott & Wicks, 1980) are adopted in this study to quantify the agreement between model results and measured data. The NRMSE represents the mean of the squared errors with respect to the range of the measured data. The index of agreement provides a dimensionless number, bounded by 0 (complete disagreement) and 1 (perfect agreement), as a measure of similarity of the trend and absolute accuracy between measured data and model results. The index of agreement is defined as

$$IA = 1 - \frac{\sum_{j=1}^{n} \left(M_j - O_j\right)^2}{\sum_{j=1}^{n} \left(\left|M_j - \overline{O}\right| + \left|O_j - \overline{O}\right|\right)^2}, \tag{21}$$

where the subscript “j” denotes jth data point in space or time, O_j represents measured data, and M_j represents model results. The variable $\overline{O}$ represents the averaged value of O_j.

10.1029/2018JC013930

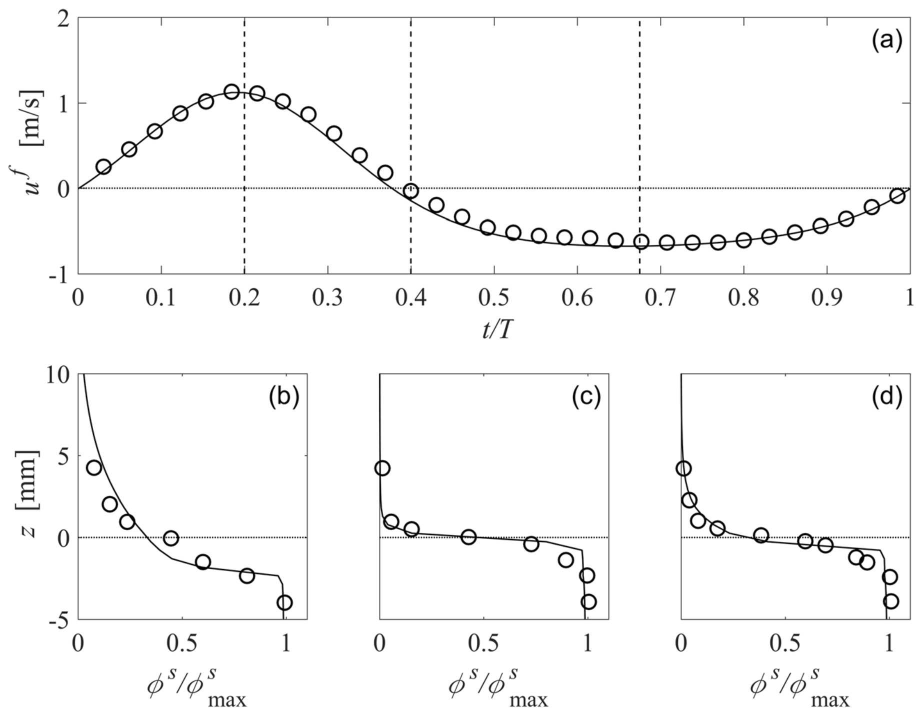

Figure 3. (a) Measured (symbols) and modeled (curves) time series of streamwise fluid velocity u^f at $x = 0$ and $z = 0.109$ m. (b–d) Comparison of vertical profiles of ϕ^s/ϕ^s_{max} at $t/T = 0.2$ (wave crest), $t/T = 0.4$ (flow reversal), and (d) $t/T = 0.675$ (wave trough), respectively.

Figure 3a shows the model-data comparison of streamwise fluid velocity, u^f, time series at $x = 0$ and $z = 0.109$ m. The flow velocity at this location is considered to be sufficiently high above the WBBL, and it is often used as the free-stream velocity to drive the 1DV bottom boundary layer models (e.g., Kranenburg et al., 2013; see also section 3.3). The overall agreement of streamwise flow velocity between model results and measured data was excellent (IA = 0.998 and NRMSE = 0.2%). Small discrepancies were found during the wave trough possibly due to the simplified model domain. From the shape of u^f time series (Figure 3a), it is evident that the wave velocity is skewed, namely, larger (smaller) velocity magnitude but shorter (longer) duration during the crest (trough). This feature is well captured by the numerical model. The velocity skewness and acceleration skewness are calculated as $\langle (u^f)^3\rangle/\langle (u^f)^2\rangle^{3/2}$ and $\langle (\partial u^f/\partial t)^3\rangle/\langle (\partial u^f/\partial t)^2\rangle^{3/2}$, respectively, where $\langle\rangle$ represents a time-averaging operator over one wave period. The velocity skewness and acceleration skewness were 0.39 (0.55) and -0.07 (-0.04) from the model results (measured data).

The vertical profiles of ϕ^s/ϕ^s_{max} at wave crest, near flow reversal, and wave trough are compared (Figures 3b–3d). The agreements between the measured and modeled sediment concentration profiles are very good (IA = 0.983, NRMSE = 0.8% under the wave crest; IA = 0.995, NRMSE = 0.3% near the flow reversal; and IA = 0.988, NRMSE = 0.7% under the wave trough). Model results indicate that the amount of mobilized sediment is almost directly associated with the magnitude of streamwise flow velocity above the WBBL, consistent with that observed in the physical experiment (Dohmen-Janssen & Hanes, 2002).

The skewness of the sheet flow transport due to the skewness in intrawave flow velocity is clearly observed in the time series of ϕ^s/ϕ^s_{max} at different vertical elevations (Figure 4). The modeled concentration at each vertical elevation is averaged over adjacent vertical grid points so that the vertical sampling height (1 mm) is consistent with that of CCM (Dohmen-Janssen & Hanes, 2002). Both the measured and modeled sediment concentrations below $z = -4$ mm are near ϕ^s_{max} and invariant in time, indicating that $z = -4$ mm is already in the immobile bed. In general, the model results show good agreements in the pickup layer ($z < 0$) with IA = 0.698, NRMSE = 1.0% at $z = -2.4$ mm and IA = 0.873, NRMSE = 2.3% at $z = -1.4$ mm, respectively. But the temporal variation at the initial bed level (IBL, $z = 0$) was less satisfactory (IA = 0.287, NRMSE = 12.7%). Unlike that in the physical experiment (Dohmen-Janssen & Hanes, 2002), the modeled

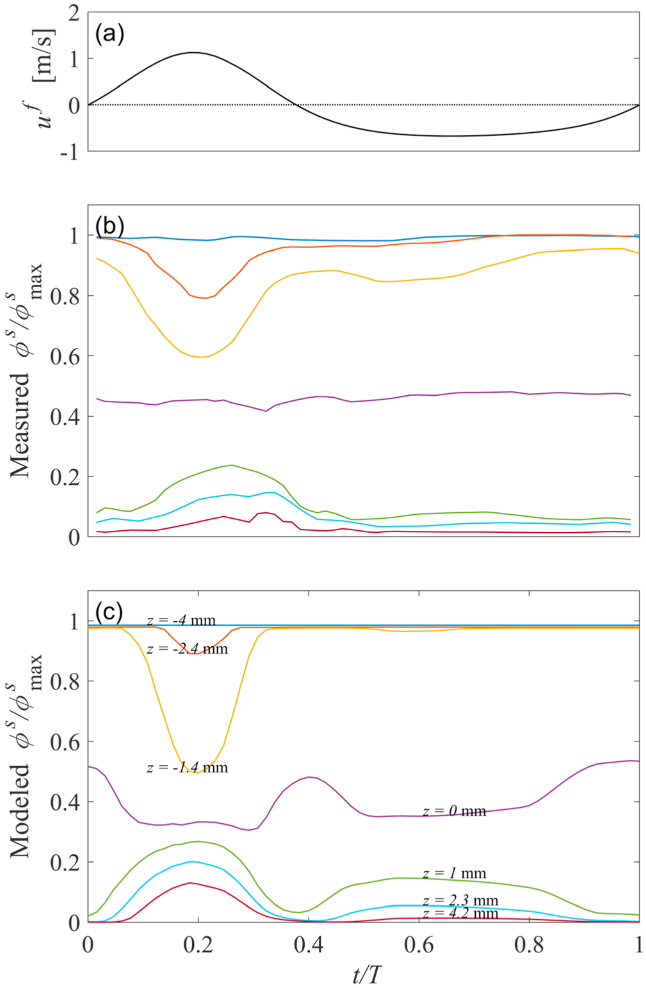

Figure 4. Time series of (a) modeled u^f at $x = 0$ and $z = 0.109$ m, and (b) measured and (c) modeled time series of ϕ^s/ϕ^s_{max} at different vertical elevations at $x = 0$.

concentration shows more significant temporal fluctuation of ϕ^s/ϕ^s_{max} at $z = 0$. It should be noted that most of the model parameters applied here (except the empirical coefficient B) were calibrated with OWT data of O'Donoghue and Wright (2004a) discussed in Cheng et al. (2017) where the fluctuations of ϕ^s time series near the IBL were slightly larger. Further model improvement on this issue for simulating large wave flume data is warranted. The magnitude and pattern of ϕ^s/ϕ^s_{max} in the sediment suspension layer ($z > 0$) are captured well by the model, and *IA*s (NRMSEs) are 0.745 (2.3%), 0.666 (2.3%), and 0.614 (1.5%) at $z = 1$, 2.3, 4.2 mm, respectively. In general, the agreement in temporal evolution of sediment concentration is very good during wave crest while larger discrepancy is observed during wave trough.

Overall, the model predicts the vertical profile of wave-averaged sediment concentration ($\langle\phi^s\rangle/\phi^s_{max}$) very well in the moderate to highly concentrated region ($\langle\phi^s\rangle/\phi^s_{max} > 0.002$) with $IA = 0.948$ and NRMSE = 2.7% (Figure 5). In the dilute region, the predicted concentration is less satisfactory compared to ABS data (crosses in Figure 5). However, sediment concentration in the dilute region is less than about 0.1% (or 3 g/L) and the model results suggest that the sediment flux with concentration greater than $\langle\phi^s\rangle/\phi^s_{max} = 0.002$ accounts for 99.9% of the total sediment transport rate. Therefore, the contribution of total sediment flux in the dilute region can be considered negligible. The model is capable of predicting the full profile of sediment concentration in wave-driven sheet flow with good accuracy. Amoudry et al. (2005) demonstrated that varying the Schmidt number σ_c may have an effect on suspended sediment concentration. However, we carried out numerical experiments by varying σ_c and found that the effect was minor and cannot explain the suspended sediment concentration measured by ABS.

3.3. Isolating the Free Surface Effect

In the present SedwaveFoam simulation of sheet flow driven by nonbreaking nonlinear waves, the velocity time series near the top of the WBBL show high-velocity skewness (see Figure 3a). Therefore, it is expected that the effects of waveshape streaming and progressive wave streaming coexist. To make an attempt to isolate these two effects, we carry out an 1DV SedFoam simulation with vertical grid resolution and model parameters identical to SedWaveFoam. As discussed, SedFoam is a boundary layer sediment transport model, which has the same capability in resolving sediment transport as SedWaveFoam except that the free surface cannot be included. Therefore, the 1DV SedFoam results represent typical data obtained from OWT experiment, and they were contrasted with SedWaveFoam results to isolate the free surface effect on the sediment transport. The flow in the SedFoam is driven by a prescribed streamwise pressure gradient (f_{ext}). The local acceleration ($\partial u^f/\partial t$) is calculated using the streamwise flow velocity (u^f) of SedWaveFoam at $z = 0.15$ m since that elevation is sufficiently away from the WBBL. Following the boundary layer approximation, f_{ext} was imposed as $f_{ext} = -\partial p^f/\partial x = \rho^f \partial u^f/\partial t$. By comparing the computational time, a 1DV SedFoam is about 2 order of magnitude more efficient than a 2DV SedWaveFoam simulation.

The results of SedWaveFoam and SedFoam are compared in the next three figures (Figures 6–8) to identify the effects associated with the waveshape streaming and progressive wave streaming. The time series of u^f at $z = 0.15$ m provided by these two models agree well ($IA > 0.999$; Figure 6a) with each other. Hence, it is anticipated that the differences in near-bed flow structures and sediment transport characteristics between them are solely due to the existence of free surface. It is clear that the vertical profiles of u^f in SedWaveFoam is slightly more onshore-directed at both the wave crest and wave trough (Figures 6b and 6c). Qualitatively, this is expected because of the onshore-directed progressive wave streaming. Moreover, we observe that both models show larger TKE under the wave crest owing to turbulence asymmetry (Figures 6e and 6f) and this

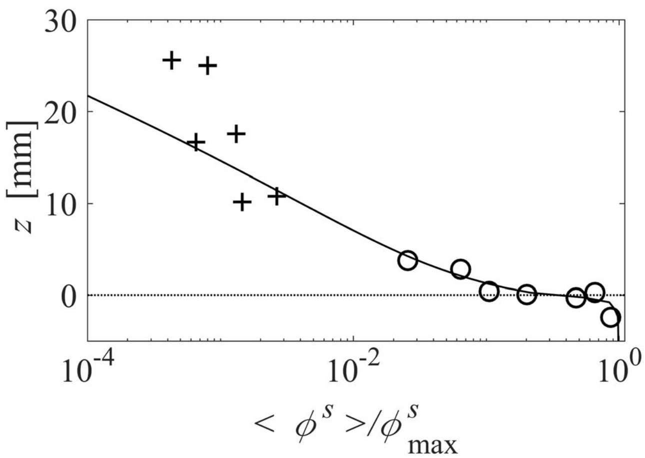

Figure 5. Wave-averaged ϕ^s/ϕ^s_{max} at x = 0 (measured data by CCM, circles; measured data by ABS, plus signs; model results, solid curve).

feature should lead to waveshape streaming (i.e., offshore-directed streaming current). By examining the vertical profiles of wave-averaged streamwise velocity, $\langle u^f \rangle$ (see Figure 6d), we clearly observe offshore-directed currents produced by both SedFoam and SedwaveFoam, which have very similar magnitudes of about -0.08 m/s away from the bed. Closer to the bed, however, it is evident that the offshore-directed current, $\langle u^f \rangle$, in SedWaveFoam is significantly weaker than that of SedFoam. This can be attributed to the competing effect from onshore-directed current due to progressive wave streaming, which can only exist in SedWaveFoam. The effect of progressive wave streaming on $\langle u^f \rangle$ can be better illustrated by simply subtracting u^f profile of SedFoam from that of SedWaveFoam instantaneously and then carry out wave-average over the resulting velocity difference (i.e., $\langle u^f_{\mathrm{SedWaveFoam}} - u^f_{\mathrm{SedFoam}} \rangle$). We observe that this mean current due to the velocity difference is indeed onshore-directed (dash-dotted curve in Figure 6d) with a peak velocity of 4.4 cm/s in the middle of the WBBL (z = 2.4 cm). This onshore-directed streaming current diminishes rapidly away from the WBBL. However, it should be reminded that the waveshape streaming plays a significant role in this case, and hence, the net steaming current in SedWaveFoam remained to be offshore-directed. Lastly, it is noted that the small onshore-directed $\langle u^f \rangle$ of several cm/s below the IBL (z = 0) can be only captured by the present two-phase models because it occurs in the concentrated region of sediment transport due to velocity skewness. This point will be illustrated more clearly next.

Figure 7 presents the vertical profiles of sediment volumetric concentrations, ϕ^s, (first row), streamwise sediment velocity, u^s, (second row), and streamwise sediment fluxes, $\phi^s u^s$, (third row) under the wave crest (column 1), wave trough (column 2), and the corresponding wave-averaged profiles (column 3). In more concentrated region ($\phi^s > 10^{-1}$), sediment concentrations from these two models are nearly identical. However, under the wave crest, the effect of free surface (SedWaveFoam results) generates higher sediment suspension away from the bed (Figure 7a) and notably larger u^s (Figure 7d), which leads to larger onshore-directed sediment flux (see Figure 7g; peak value of $\phi^s u^s$ from SedWaveFoam is 8.9 cm/s, which is 11.9% larger than that of SedFoam). In contrast, this trend is opposite under the wave trough, and SedFoam shows slightly larger offshore flux (increased by 8.4%; see Figure 7h). Wave-averaged streamwise sediment velocity, $\langle u^s \rangle$, has a weaker offshore-directed current in SedWaveFoam results (solid curve in Figure 7f). Moreover, the wave-averaged streamwise sediment velocity difference (i.e., $\langle u^s_{\mathrm{SedWaveFoam}} - u^s_{\mathrm{SedFoam}} \rangle$) also shows the onshore-directed current (dash-dotted curve in Figure 7f) due to the progressive wave streaming, consistent with Figure 6d. The maximum $\langle u^s_{\mathrm{SedWaveFoam}} - u^s_{\mathrm{SedFoam}} \rangle$ is obtained as 4.5 cm/s at z = 27.9 mm. More importantly, below the IBL ($z < 0$), $\langle u^s \rangle$ becomes onshore-directed, which leads to significant onshore sediment flux near and below the IBL (see Figure 7i). However, $\langle u^s_{\mathrm{SedWaveFoam}} - u^s_{\mathrm{SedFoam}} \rangle$ is relatively small (about 1 cm/s) below the IBL ($z < 0$), suggesting limited progressive wave streaming effect. Qualitatively, this onshore flux in the concentrated region of transport is known in the literature as the bedload flux associated with wave velocity skewness (Ribberink, 1998). It is worthwhile to point out that the wave-averaged sediment fluxes above the IBL are also onshore-directed for both models even though mean current $\langle u^s \rangle$ is offshore directed. This implies that the net onshore flux is mainly driven by intrawave process and this point will be discussed in more details later. From Figure 7i, we observe that the free surface effect enhances net onshore flux throughout the entire sheet flow layer and the effect is more pronounced above the IBL.

The temporal evolutions of bed shear stress (τ_b), WBBL thickness (δ_w), sheet flow layer thickness (δ_s), and sediment transport rate (q^s) with reference to the time series of u^f at the top of WBBL (z = 45.6 mm) are shown in Figure 8. In the present two-phase model, the total shear stress is calculated by the sum of the fluid shear stress and particle shear stress. Here the total bed shear stress τ_b is evaluated at a fixed vertical location of IBL (z = 0). This choice is consistent with typical single-phase suspended load models (e.g., van Rijn, 1987), and therefore, it is easier to see the implication of the present model results to sediment transport parameterization (see section 4). Although τ_b time series obtained from SedWaveFoam and SedFoam are similar, the free surface effect clearly shifts τ_b of SedWaveFoam to be more onshore-directed due to progressive wave

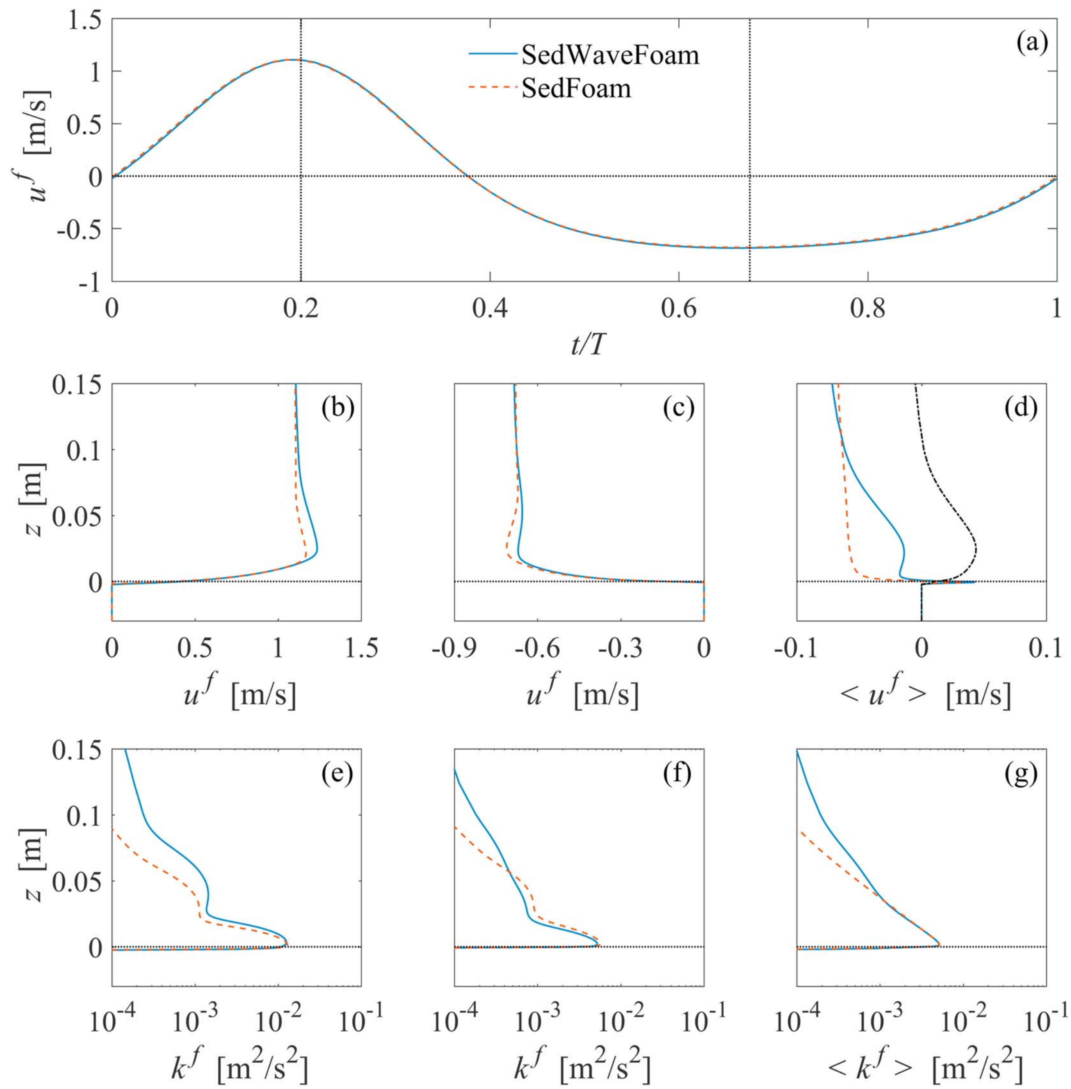

Figure 6. Model comparisons of fluid phase characteristics (SedWaveFoam: blue solid curves; SedFoam: red dashed curves). (a) Time series of u^f at z = 0.15 m. (b and e) Vertical profiles of u^f and k^f under wave crest (t/T = 0.2), and (c and f) those under wave trough (t/T = 0.675). (d and g) Wave-averaged vertical profiles of u^f and k^f. The black dash-dotted curve in (d) represent $u^f_{\text{SedWaveFoam}} - u^f_{\text{SedFoam}}$.

streaming. Looking into the details, this onshore-directed enhancement is more pronounced under the wave crest. The peak value of τ_b from SedWaveFoam is 6.12 Pa under the wave crest, and it is increased by 0.64 Pa (11.9%) comparing to SedFoam results due to progressive wave streaming. On the other hand, the difference in τ_b during wave trough is much smaller. Overall, the wave-averaged bed shear stress ($\langle \tau_b \rangle$) from SedWaveFoam was increased by only 0.17 Pa compared to that of SedFoam. This finding suggests that the onshore contribution of τ_b enhanced by progressive wave streaming is highly uneven in the intrawave time scale. Its implication to sediment transport parameterization will be investigated later. It should also be noted that a phase lead of τ_b is observed comparing with u^f (φ = 13.3° for both models). This phase lead, φ, between τ_b and u^f in the WBBL is well known in the literature (e.g., Nielsen, 2002, 2006; Nielsen & Callaghan, 2003).

The instantaneous elevation of the top of WBBL ($z = z_w$) is defined at the vertical location where the peak value in the u^f profile occurs due to overshoot (Jensen et al., 1989; O'Donoghue & Wright, 2004b). In addition, the instantaneous bed location (z_{bed}) is defined at where sediment velocity is smaller than a very small threshold velocity of 10^{-4} m/s ($|u^s| < 10^{-4}$ m/s). Then, the instantaneous WBBL thickness (δ_w) is defined as

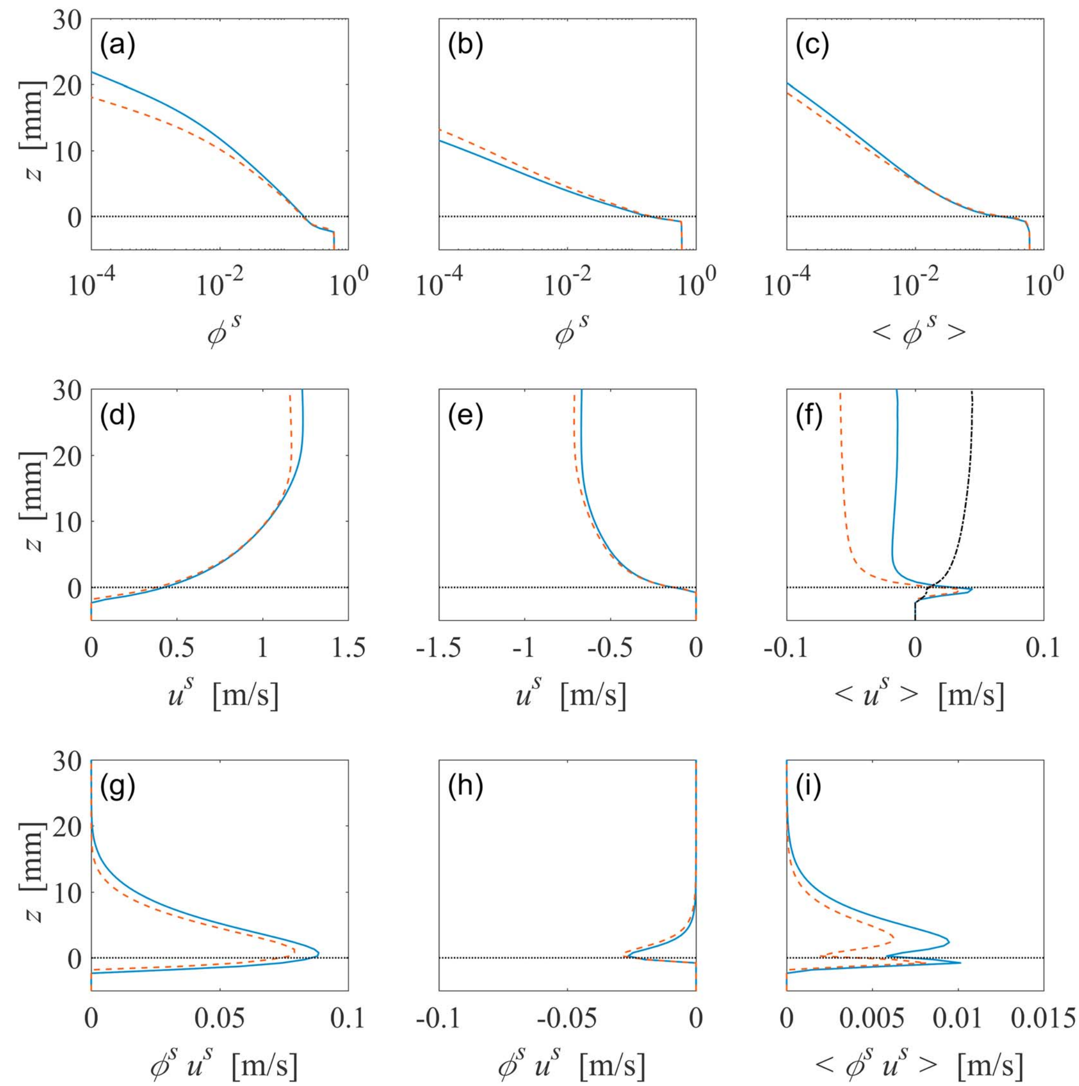

Figure 7. Model comparisons of sediment phase characteristics (SedWaveFoam: blue solid curves; SedFoam: red dashed curves). (a, d, and g) Vertical profiles of ϕ^s, u^s, and $\phi^s u^s$ under wave crest ($t/T = 0.2$), and (b, e, and h) those under wave trough ($t/T = 0.675$). (c, f, and i) Wave-averaged vertical profiles of ϕ^s, u^s, and $\phi^s u^s$. The black dash-dotted curve in (f) represent $u^s_{\mathrm{SedWaveFoam}} - u^s_{\mathrm{SedFoam}}$.

$\delta_w = z_w - z_{\mathrm{bed}}$. Near the flow reversal ($0.86 < t/T < 0.95$), the overshoot did not exist, and hence, z_w could not be identified in SedWaveFoam. The magnitudes of WBBL thickness in both models are very similar (see Figure 8c). SedWaveFoam results show slightly larger δ_w (10.5%) during the positive phase (t/T = 0–0.4) compared to SedFoam results (Figure 8c) due to larger turbulence (see Figure 6e). In general, δ_w is smaller under the positive phase for both models than that under the negative phase because the positive phase (wave crest) has relatively shorter time to develop owing to the skewed waveshape. We can observe that progressive wave streaming has small effect on WBBL thickness. The elevation of the top of sheet flow layer (z_s) is defined at location where $\phi^s = 0.08$ (Bagnold, 1954). We then define the sheet flow layer thickness (δ_s) as $\delta_s = z_s - z_{\mathrm{bed}}$. Sheet flow layer thickness δ_s calculated from SedWaveFoam results is 6.25 mm under the wave crest and 2.08 mm under the wave trough (Figure 8d). These values agree well with the measured data (6 ± 1 mm for wave crest; 2.75±0.25 mm for wave trough). Without progressive wave streaming, SedFoam results show smaller δ_s (5.72 mm for wave crest and 2.08 mm for wave trough). Again, the effect of progressive wave streaming on sheet flow layer thickness is not significant.

Time-dependent total sediment transport rate, q^s, is calculated by integrating the horizontal sediment flux over the water column at a given time:

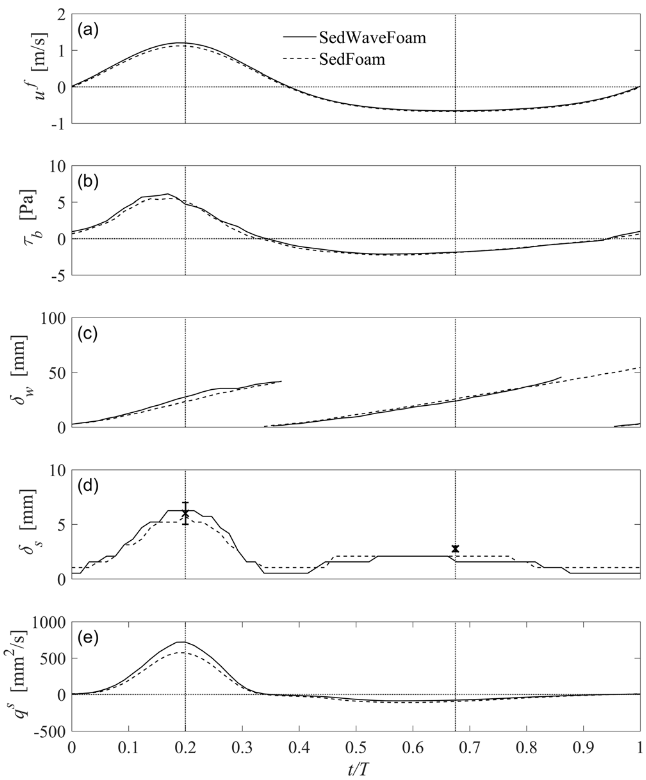

Figure 8. Time series of (a) u^f at the top of WBBL (free-stream velocity), (b) τ_b, (c) δ_w, (d) δ_s, and (e) q^s (SedWaveFoam: solid curves; SedFoam: dashed curves; measured data: symbols in Figure 8d).

$$q^s(t) = \int_{z_{\mathrm{bed}}(t)}^{\eta(t)} \phi^s(z,t) u^s(z,t) dz, \tag{22}$$

in which η is the elevation of the free surface (for SedWaveFoam) or the top of the model domain (for SedFoam). Under the wave crest, SedWaveFoam results indicate an enhanced q^s compared with that of SedFoam (25.7%), while a slightly reduced q^s in offshore direction is observed during wave trough (Figure 8e). As a result, there is an increased net onshore flux in the SedWaveFoam results. This comparison clearly shows that progressive wave streaming plays a significant role in driving onshore sediment transport. However, the enhanced onshore sediment transport rate is highly time dependent. The onshore enhancement of q^s due to the progressive wave streaming is more pronounced under the wave crest than that during the wave trough. Specifically, onshore sediment transport associated with progressive wave streaming is larger when intrawave velocity is more intense, which may indicate some nonlinear wave-stirring effects. By examining the time series in more details in Figure 8, we also observe notable phase lags of δ_s and q^s with respect to τ_b (both are 11.1° for SedWaveFoam and 11.6° for SedFoam). Dohmen-Janssen et al. (2002) quantified the phase lag effect with a phase lag parameter, which is due to the lag time of suspended sediment to re-settle to the bed versus the wave period. For fine sand ($d_{50} < 0.15$ mm), this phase lag effect can be very substantial to cause offshore sediment transport under a velocity skewed wave. Here for medium sand, we observe a phase lag of about 11° for both q^s and δ_s with respect to τ_b. Interestingly, since there is a phase lead between τ_b and the free-stream velocity, the resulting phase difference between free-stream velocity and q^s (or δ_s) becomes almost negligible (only about 2°). Although the near cancelation between phase lead and phase lag observed here is a coincidence, this is consistent with the finding reported by Dohmen-Janssen et al. (2002). Namely, the phase lag parameter, $\alpha\delta_s\omega/w_s$ where α is a calibration coefficient, w_s is the settling velocity, and ω is the angular frequency, in the present case is about 0.23. This is much smaller than unity, and the quasi-steady approach is applicable (i.e., negligible phase difference between free-stream velocity and sediment transport rate).

The measured wave-averaged total sediment transport rate (net transport rate), $\langle q^s \rangle$, is 42.9 ± 17.2 mm^2/s using the bed level change (multiple transducer array) and is 70.7 ± 35.4 mm^2/s using the extrapolated sediment fluxes (Dohmen-Janssen & Hanes, 2002). The modeled $\langle q^s \rangle$ from SedWaveFoam is 80.3 mm^2/s, which is 59.4% larger than that from SedFoam (50.4 mm^2/s). Based on the various time series shown in Figure 8, we observe an interesting feature that requires further investigation. Onshore sediment transport rate due to progressive wave streaming is enhanced by nearly 60%. However, the differences in the time series of τ_b, δ_w, and δ_s between SedWaveFoam and SedFoam results are surprisingly small. To be specific, the difference of wave-averaged τ_b between SedWaveFoam and SedFoam was only 0.17 Pa (2.8% of the peak value under the crest). Similarly, the difference of τ_b between SedWaveFoam and SedFoam during wave crest (trough) was 0.64 Pa (0.13 Pa), which is about 10.5% (2.2%) of the peak value. Therefore, some nonlinear amplification mechanisms of transport rate at the intrawave timescale must exist.

To demonstrate the importance of intrawave sediment transport, the wave-averaged sediment flux ($\langle \phi^s u^s \rangle$) can be decomposed into the current-induced sediment flux ($\langle \phi^s \rangle \langle u^s \rangle$) and wave-induced sediment flux $\left(\left\langle \widetilde{\phi}^s \widetilde{u}^s \right\rangle \right)$ where $\widetilde{\ }$ represents the demeaned (intrawave) quantity, and we define $\phi^s(t) = \langle \phi^s \rangle + \widetilde{\phi}^s(t)$ and $u^s(t) = \langle u^s \rangle + \widetilde{u}^s(t)$. While both SedWaveFoam and SedFoam model results show a similar trend, the onshore flux is much stronger in SedWaveFoam results (Figure 9a). It is also clear that progressive wave streaming enhances onshore sediment transport more significantly in the suspended load region. For instance, wave-averaged sediment transport rate of SedWaveFoam was increased by 24.4% in the concentrated region below the IBL (z = 0), while it is increased by 50.7% above the IBL. Additionally, both model

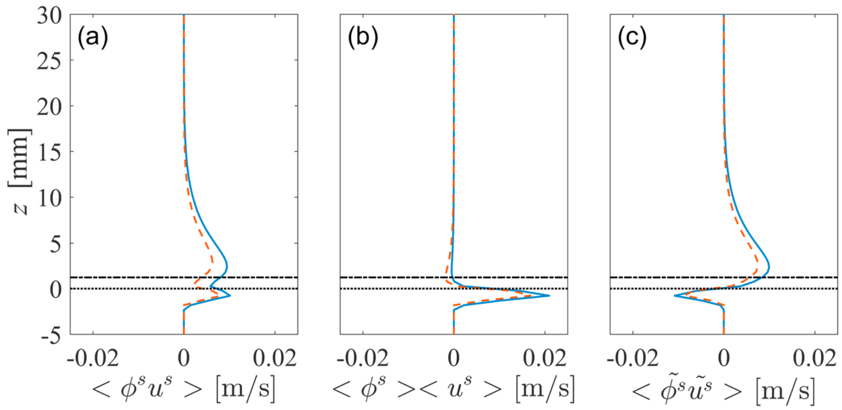

Figure 9. Contributions to (a) $\langle \phi^s u^s \rangle$ from (b) $\langle \phi^s \rangle \langle u^s \rangle$ and (c) $\widetilde{\phi^s}\,\widetilde{u^s}$ of SedWaveFoam (blue solid curves) and SedFoam (red dashed curves). The black dash-dotted lines represent $\langle z_s \rangle$ = 1.2 mm.

results indicate distinctly different vertical distributions of wave-averaged sediment fluxes associated with the current-induced component and wave-induced component. The current-induced components in both models are mostly onshore-directed but mainly occurred in the concentrated region below the IBL (Figure 9b). On the other hand, wave-induced components in both models show offshore-directed transport below the IBL, while a large amount of onshore-directed transport is occurring above the IBL in the suspended load region (Figure 9c).

In summary, additional onshore sediment transport associated with progressive wave streaming mostly takes place in the suspended load region (transport occurs above the IBL) in the intrawave component. This may explain why previously we discovered that increased onshore sediment transport associated with progressive wave streaming was much larger than the increase of wave-averaged bed shear stress. The large intrawave component in the suspended load region may be attributed to a wave-stirring effect (Figure 10). Wave-stirring effect has been used to describe enhanced sediment transport driven by mean current (e.g., tidal current and undertow) due to high turbulence in the WBBL (e.g., Soulsby, 1997). In the present case, we extend this concept for pure surface wave in which the "mean current" is due to the boundary layer streaming current. Namely, the intense wave motion drives large amount of sediment suspended above the IBL such that the magnitude of wave-averaged current (or enhanced bed shear stress due to progressive wave streaming) does not need to be very large to drive large sediment transport rate. This finding shall provide guidance for sediment transport parameterization to be discussed in section 4.

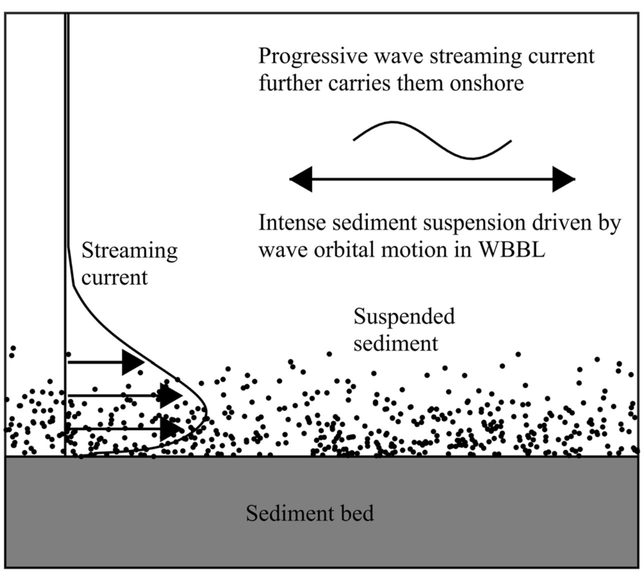

Figure 10. Definition sketch of wave-stirring mechanism in wave-averaged formulation under surface waves.

4. Parameterization

Using the model results from SedWaveFoam and SedFoam, we investigate key intrawave features in bed shear stress (τ_b), sheet flow layer thickness (δ_s), and sediment transport rate (q^s) in order to infer efficient parameterizations of these sediment transport quantities.

4.1. Bed Shear Stress

To parameterize sediment transport, the typical first step is to parameterize the bed shear stress. Particularly, one first needs to calculate the progressive wave streaming-induced wave-averaged bed shear stress, $\langle \tau_{\mathrm{pws}} \rangle$ (e.g., Nielsen, 2006). From the present model results, we can compute $\langle \tau_{\mathrm{pws}} \rangle$ by subtracting $\langle \tau_b \rangle$ obtained with SedFoam from $\langle \tau_b \rangle$ obtained with SedWaveFoam (i.e., $\langle \tau_{\mathrm{pws}} \rangle = \langle \tau_{b,\ \mathrm{SedWaveFoam}} \rangle - \langle \tau_{b,\ \mathrm{SedFoam}} \rangle$) to isolate the progressive wave streaming component. The resulting value is $\langle \tau_{\mathrm{pws}} \rangle$=0.17 Pa.

In the literature, the $\langle \tau_{\text{pws}} \rangle$ is estimated by wave energy dissipation rate divided by wave phase speed (e.g., Longuet-Higgins, 2005;Nielsen, 2006 ; Nielsen & Callaghan, 2003):

$$\left\langle \tau_{\text{pws}} \right\rangle = \frac{2}{3\pi} \rho^f f_w k A^3 \omega^2, \tag{23}$$

where k is the wave number. Following Nielsen (1992), the wave dissipation factor (same as wave friction factor), f_w, can be estimated as

$$f_w = \exp\left[5.5 \left(\frac{k_s}{A}\right)^{0.2} - 6.3\right], \tag{24}$$

where k_s is the bed roughness, and semiexcursion length, A, is given by $A = \sqrt{2} U_{\text{rms}}/\omega$. There is a debate regarding the choice of the bed roughness to determine $\langle \tau_{\text{pws}} \rangle$ (Nielsen, 2006; Nielsen & Callaghan, 2003). Here the typical k_s = 2.5d_{50} gives a value of $\langle \tau_{\text{pws}} \rangle$ = 0.20 Pa, which is close to the present model result of 0.17 Pa. In contrast, a considerably increased k_s was suggested by Nielsen and Callaghan (2003) based on the energy dissipation data for rough flat beds (Carstens et al., 1969) as

$$k_s = 170 \sqrt{\theta_{2.5} - 0.05} d_{50}, \tag{25}$$

where $\theta_{2.5}$ is obtained as $\theta_{2.5} = 0.5 f_{2.5} (A\omega)^2 / [(s - 1) g d_{50}]$ following Nielsen (1992). In the present case, k_s calculated by equation (25) gives 136d_{50}, and the corresponding $\langle \tau_{\text{pws}} \rangle$ using equation (23) would be 0.95 Pa. This value is significantly larger than that suggested here, and using a large roughness suggested by equation (25) to estimate $\langle \tau_{\text{pws}} \rangle$ is inconsistent with SedWaveFoam/SedFoam results. It should be pointed out that this $\langle \tau_{\text{pws}} \rangle$ is further added to bed shear stress and it is plugged into a power law to estimate the corresponding net transport rate (Nielsen, 2006). Using this direct approach without explicitly considering the intrawave wave-stirring effect may indeed require a significantly enhanced bed shear stress (or bed roughness) in order to match an expected net onshore sediment transport rate due to progressive wave streaming. In fact, according to Figure 8a, the noticeable increase of q^s occurs as a sudden burst under the wave crest associated with large intrawave velocity. According to the present model results, the significant onshore sediment transport due to progressive wave streaming is not directly related to enhanced bed shear stress but is mainly associated with transport fluxes due to nonlinear interaction among waves, streaming currents, and the resulting sediment suspension. The proper inclusion of wave-induced streaming in the parameterization of sediment transport rate will be discussed in section 4.3.

Adequate parameterization of time-dependent bed shear stress is investigated by comparing SedFoam and SedWaveFoam results with several commonly used simpler approaches. Without considering the progressive wave streaming effect, a couple of simpler methods are first compared with SedFoam results (Figure 11). The simplest parameterization to predict the bed shear stress is a quasi-steady approach:

$$\tau_b = \frac{1}{2} \rho^f f_w u_\infty^f \left| u_\infty^f \right|, \tag{26}$$

where f_w is calculated by equation (24) and the corresponding k_s is obtained either by using a mobile bed roughness formulation (Ribberink, 1998) or being adjusted to match with the measured data. Here the best fit k_s comparing with time series of τ_b from SedFoam is obtained as 7.3d_{50} based on the lowest NRMSE. Comparing to SedFoam results, τ_b predicted by the quasi-steady approach is completely in phase with free-stream velocity. Because the phase lead cannot be captured in this approach, the agreement is less satisfactory in the comparison (IA = 0.969, NRMSE = 8.4%; Figure 11b). Moreover, although τ_b matches the peak value under the wave crest with 1.1% error, the peak value under the wave trough was under predicted by about 10.5% (blue dashed curve in Figure 11a). According to SedFoam result, the quasi-steady approach slightly overestimates the skewness of bed shear stress in sheet flows.

To capture the phase lead of τ_b in WBBL, a single-phase 1DV WBBL model can be considered. The 1DV WBBL model adopted here solves the single-phase Reynolds-average Navier-Stokes equation with a two-equation k-ε turbulence closure following the boundary layer approximation. Similar to SedFoam, the single-phase

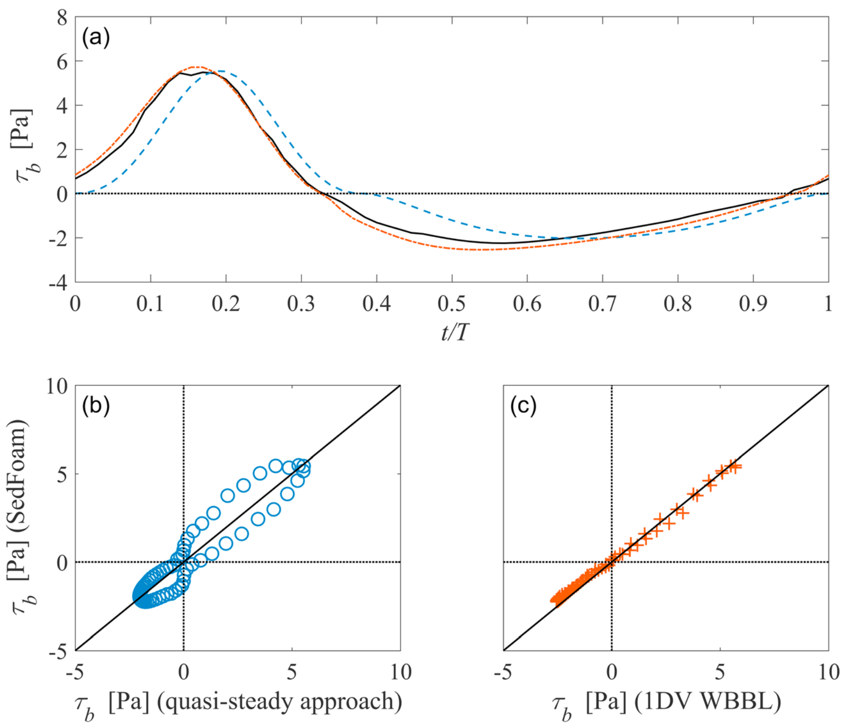

Figure 11. (a) Time series of τ_b from SedFoam (black solid curve) compares with that calculated from the quasi-steady approach (blue dashed curve) and single-phase 1DV WBBL model (red dash-dotted curve). (b and c) Agreement between τ_b of SedFoam versus τ_b computed by the quasi-steady approach and the single-phase 1DV WBBL model, respectively.

1DV WBBL model is also designed to model OWT condition. The single-phase 1DV WBBL adopts logarithmic law for rough bed as bottom boundary condition:

$$\frac{u^f}{u_*} = \frac{1}{\kappa} \ln\left(\frac{30z}{k_s}\right), \tag{27}$$

where κ is the von Karman constant (κ = 0.4) and instantaneous bed shear stress can be calculated as $\tau_b = \rho^f u_* |u_*|$. Here we specify $k_s = 7.3d_{50}$, consistent with the quasi-steady approach. The computational cost of the single-phase 1DV WBBL model is significantly less than those of SedFoam and SedWaveFoam. The single-phase 1DV WBBL model predicts a time series of τ_b that agrees very well with that of SedFoam (*IA* = 0.997 and NRMSE = 0.9%; Figure 11c). The phase lead and the relative magnitudes of τ_b during the wave crest and wave trough are also matched well (red dash-dotted curve in Figure 11a). We note that many parameterizations have been proposed to take into account the phase lead by considering the effect of horizontal pressure gradient (or flow acceleration) into τ_b (Nielsen, 2006; Nielsen & Callaghan, 2003). However, their improvements on the agreement were not significant, and therefore, they are not further discussed here for brevity.

As demonstrated previously, equation (23) agrees well with the present numerical model results and it can be used to estimate $\langle\tau_{\mathrm{pws}}\rangle$. Here to further compare with SedWaveFoam results, $\langle\tau_{\mathrm{pws}}\rangle$ obtained using equation (23) with $2.5d_{50}$ (i.e., $\langle\tau_{\mathrm{pws}}\rangle$ = 0.20 Pa) is simply added to τ_b of the single-phase 1DV WBBL model and of SedFoam in order to predict the τ_b under surface waves (Figure 12a). Compared with the τ_b of SedWaveFoam, the $\tau_b + \langle\tau_{\mathrm{pws}}\rangle$ of the single-phase 1DV WBBL model slightly underpredicts the peak stress value under the wave crest by about 3.5% but the overall *IA* (NRMSE) 0.998 (0.7%) is very good (Figure 12b). SedFoam results show very good agreement with that of SedWaveFoam (Figure 12c) with *IA* (NRMSE) of 0.998 (0.5%). Comparisons shown here suggest that only the streamwise flow velocity input is needed for the 1DV WBBL type models (simulate OWT with free-surface) to predict the time series of bed shear stress $\tau_b + \langle\tau_{\mathrm{pws}}\rangle$ under surface waves.

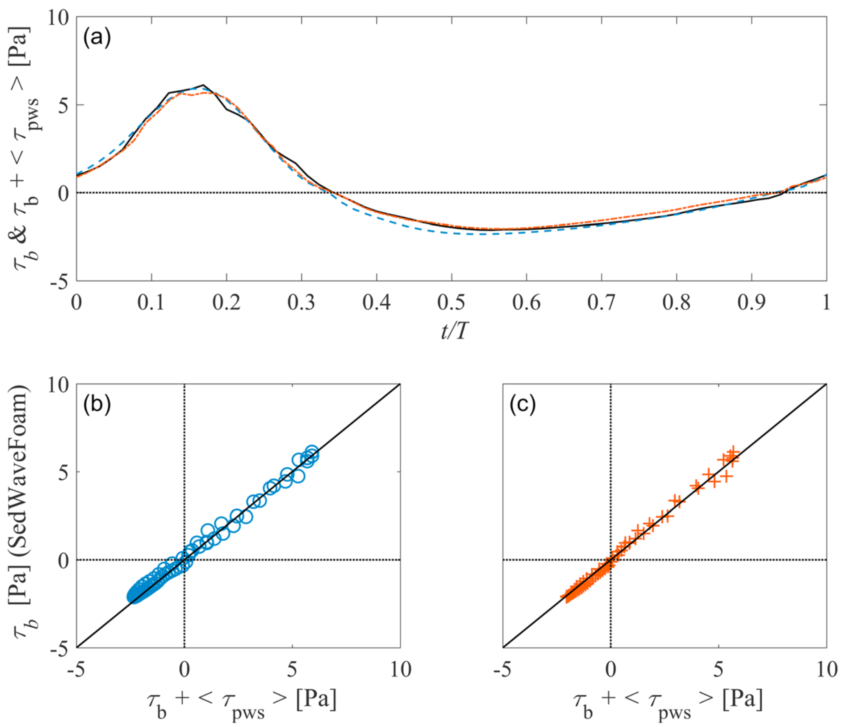

Figure 12. (a) Time series of τ_b from SedWaveFoam (black solid curve) and $\tau_b + \langle\tau_{pws}\rangle$ calculated from the single-phase 1DV WBBL model and equation (23) (blue dashed curve) and SedFoam and equation (23) (red dash-dotted curve). (b and c) Agreement between τ_b of SedWaveFoam versus $\tau_b + \langle\tau_{pws}\rangle$ of single-phase 1DV WBBL model and of SedFoam, respectively.

To further predict the temporal evolution of sheet flow layer thickness and sediment transport rate with a simple formulation, a quasi-steady formulation can be adopted using the time series of τ_b discussed here. We would like to point out that although τ_b predicted by equation (26) using the quasi-steady approach failed to capture the phase lead with respect to the free-stream velocity, further coupling equation (26) with the quasi-steady formulation to predict time-dependent sediment transport rate (or sheet flow layer thickness) may have a good predictive skill because of another phase lag between sediment transport rate (or sheet flow layer thickness) and bed shear stress as demonstrated in Figure 8. However, we must also point out that for waves under high acceleration skewness (saw-tooth waves), unsteady effect in time-dependent bed shear stress further drives onshore sediment transport (Nielsen, 2006) and the capability of equation (26) is limited. In the following, time series of bed shear stress computed by those numerical models incorporating unsteady effects and the quasi-steady formulation are used to further predict sheet flow layer thickness and sediment transport rate.

4.2. Sheet Flow Layer Thickness

A linear relationship between the maximum sheet flow layer thickness, $\delta_{s,\,\mathrm{max}}$, and maximum Shields parameter, θ_{max}, has been widely adopted to empirically relate one with another (e.g., Dohmen-Janssen et al., 2001; Mieras et al., 2017). Following Wilson (1987) and Sumer et al. (1996), it can be expressed as

$$\frac{\delta_{s,\,\mathrm{max}}}{d_{50}} = \Lambda\theta_{\mathrm{max}}, \tag{28}$$

where the maximum value of the Shields parameter (see Table 2) over one wave period with the Shields parameter, θ, defined as

$$\theta = \frac{|\tau_b|}{\rho^f(s-1)gd_{50}}. \tag{29}$$

The empirical coefficient, Λ, was originally estimated as 10–13 for the steady sheet flows (Sumer et al., 1996; Wilson, 1987). For sheet flows in OWT or under surface waves, this coefficient becomes larger.

Table 2
Key Sediment Transport Quantities Provided by Models and Measured Data

ID	SedwaveFoam (wave)	Measured	SedFoam (OWT)
δ_w under crest	27.6 mm		23.4 mm
δ_w under trough	24.0 mm	N/A	26.0 mm
$\delta_{w,\ max}$	45.6 mm		54.3 mm
δ_s under crest	6.25 mm	6 ± 1 mm	5.72 mm
δ_s under trough	2.08 mm	2.75 ± 0.25 mm	2.08 mm
$\langle q^s \rangle$	80.3 mm^2/s	42.9 ± 17.2 mm^2/s (multiple transducer array) 70.7 ± 35.4 mm^2/s (sediment flux)	50.4 mm^2/s
$\langle \tau_{\text{pws}} \rangle$	0.17 Pa	N/A	0 Pa
θ_{max}	1.58	N/A	1.41

Ribberink et al. (2008) suggested Λ to be 10.6 ±5.3 using OWT data, and Dohmen-Janssen and Hanes (2002) suggested Λ in the range of 14.3–27.8 for sheet flows driven by surface waves. Using $\delta_{s,\ \text{max}}$ and θ_{max} provided by SedWaveFoam (SedFoam), Λ is calculated to be 16.52 (16.89), consistent with previous studies. It should also be noted that Sumer et al. (1996) found a strong dependency of δ_s on the ratio of of friction velocity to settling velocity (w_s/u_*) particularly in the case of suspension mode ($w_s/u_* < 0.8 - 1$). Therefore, our finding here is only limited to the present wave condition and grain size, which gives $\langle w_s/u_* \rangle = 2.87$.

Here we further evaluate the parameterization of temporal evolutions of δ_s. As discussed previously, the time series of free-stream velocity and δ_s are almost in phase with each other (see Figures 8a and 8d). Therefore, it is useful to also include the quasi-steady parameterization of τ_b (equation (26)) in the present analysis. To calculate Shields parameter under surface waves, $\langle \tau_{\text{pws}} \rangle$ estimated from equation (23) for wave-averaged bed shear stress due to progressive wave streaming is added to the time-dependent bed shear stress, τ_b, calculated by equation (26) as $\theta' = (\tau_b + \langle \tau_{\text{pws}} \rangle)/[\rho^f(s - 1)gd_{50}]$ where superscript "′" represents the inclusion of $\langle \tau_{\text{pws}} \rangle$. Then, the relationship between time-dependent δ_s and θ' using the quasi-steady parameterization can be expressed as

$$\frac{\delta_s(t)}{d_{50}} = \Lambda \theta'(t). \tag{30}$$

Using Λ = 16.52, the agreement between the predicted sheet flow layer thickness completely based on the quasi-steady assumptions and SedWaveFoam results is good (*IA* = 0.971 and NRMSE = 22.0%; see Figure 13b). As also demonstrated in Figures 8b and 8d, a phase difference of 13.3° exists between bed shear stress and sheet flow layer thickness for SedWaveFoam. Generally, to parameterize time-dependent sheet flow layer thickness using bed shear stress obtained from numerical models that resolve unsteady effect, a phase lag φ should be further included and equation (30) becomes

$$\frac{\delta_s(t)}{d_{50}} = \Lambda \theta(t - \varphi \text{T}/2\text{n}) = \Lambda \theta(t^*), \tag{31}$$

with $t^* = t - \varphi$T/2n where superscript "*" represents the time with phase shift. Here we demonstrate the importance of including phase lag φ in predicting the temporal evolution of sheet flow layer thickness by substituting the bed shear stress computed by SedWaveFoam into equation (31). Also, using Λ = 16.52, the time-dependent sheet flow layer thickness predicted by equation (31) is compared with sheet flow layer thickness produced directly by SedWaveFoam and their agreement is very good (see Figure 13c; *IA* = 0.988 and NRMSE = 9.3%). On the other hand, if the phase lag is not included ($\varphi = 0$; see Figure 13d), the agreement is not good (*IA* = 0.945 and NRMSE = 40.1%).

To summarize, the linear relationship between sheet flow layer thickness and Shields parameter can be practically used in time-dependent parameterization. Under the surface wave, the progressive wave streaming-induced bed shear stress can be considered by adding $\langle \tau_{\text{pws}} \rangle$ using equation (23). Considering the phase

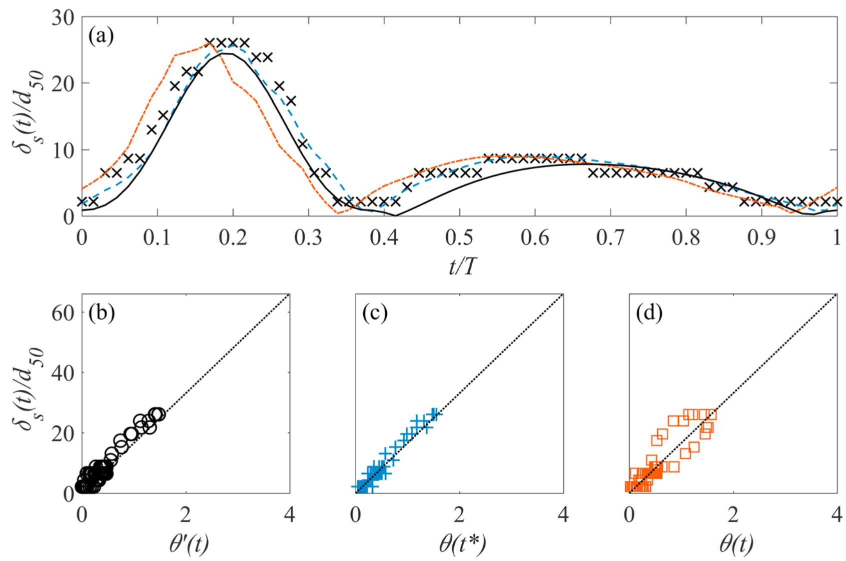

Figure 13. (a) Time series of $\delta_s(t)/d_{50}$ from SedWaveFoam (crosses) compares to the full quasi-steady approach using equations (23), (26), and (30) (black solid curve), using SedWaveFoam τ_b and equation (31) with phase lag (blue dashed curve), and using SedWaveFoam τ_b and equation (30) without phase lag (red dash-dotted curve) and panels (b), (c), and (d) show the corresponding agreement.

shift in bed shear stress (or sheet flow layer thickness) is necessary to improve the prediction of sheet flow layer thickness (or bed shear stress).

4.3. Sediment Transport Rate

Based on the bed shear stress obtained in section 4.1, we further investigate two different approaches for the parameterization of time-dependent sediment transport rate. In particular, we focus on the incorporation of wave-stirring effects associated with progressive wave streaming.

Based on an energetic concept, Bailard (1981) proposes that the time-dependent total sediment transport rate, $q^s(t)$, can be parameterized by the intrawave streamwise flow velocity (u^f) with power of 3 (or 5) for bed load (suspended load). Similarly, Ribberink et al. (2008) examined the relationship between intrawave Shields parameter, $\theta(t)$, and time-dependent bedload transport rate, $q_b^s(t)$, and proposed a bedload transport formula using a power law. For simple parameterization considered here, we assume that the power law can be extended to total load transport (Bailard, 1981) and write

$$\Phi^s(t) = \frac{q^s(t)}{\sqrt{(s-1)gd^3}} = m_b[\theta(t) - \theta_c]^n, \tag{32}$$

where θ_c is the critical Shields parameter (Van Rijn, 1993), Φ^s is the nondimensional total sediment transport rate. It is noted here that the best fit empirical coefficients $m_b = 11$ and $n = 1.65$ are obtained for the bedload transport driven by oscillatory flows (Ribberink, 1998; Ribberink et al., 2008). The best fit value of coefficient n with time series of sediment transport rate computed by SedFoam is 1.64, fairly close to the value proposed by Ribberink (1998). Hence, we follow Ribberink (1998) and $n = 1.65$ is selected here.

As discussed previously in section 3.3 (Figures 8a and 8e), the free-stream velocity and the time-dependent sediment transport rate are nearly in-phase. In this case, bed shear stress parameterized by the quasi-steady formula (equation (26)) is directly substituted to equation (32). With a best fit value of $m = 23.7$, the agreement between Φ^s of SedFoam and that predicted by the quasi-steady approach is very good ($IA = 0.994$ and NRMSE = 8.2%; see Figures 14a and 14b). The predicted $\langle\Phi^s\rangle$ with equation (32) using the quasi-steady approach is 3.03, which is close to the SedFoam result of $\langle\Phi^s\rangle = 3.37$.

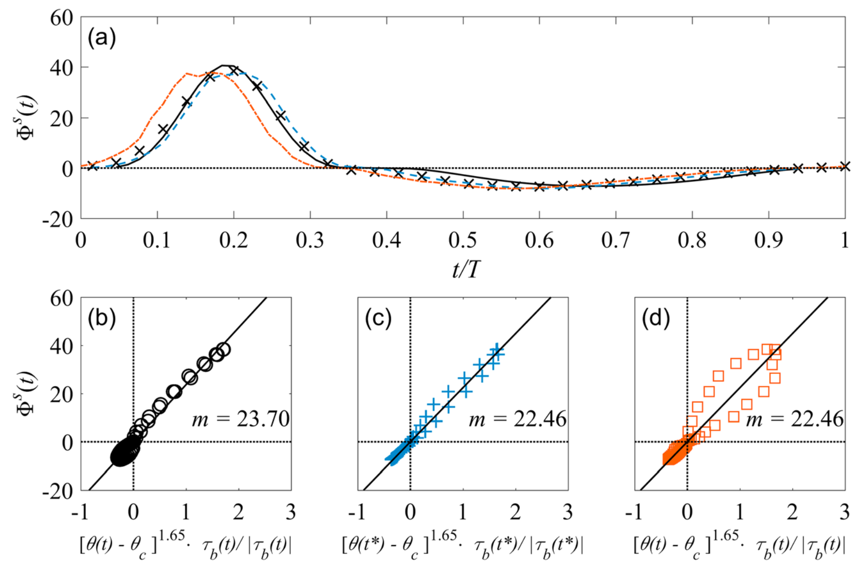

Figure 14. (a) Time series of $\Phi^s(t)$ computed by SedFoam is compared with those parameterized by equation (32) (full quasi-steady approach: black solid curve), SedFoam τ_b and equation (33) with φ = 13.3° (blue dashed curve), and SedFoam τ_b and equation (32) without phase lag (red dash-dotted curve) and panels (b), (c), and (d) show the corresponding agreement.

We also demonstrated previously (Figures 8b and 8e) that a phase difference exists between bed shear stress and sediment transport rate in the SedFoam results. Therefore, to model the time-dependent sediment transport rate using the time series of bed shear stress obtained from SedFoam, a phase shift of φ = 13.3° needs to be added in equation (32):

$$\Phi^s(t) = m[\theta(t^*) - \theta_c]^n \ \tau_b(t^*)/|\tau_b(t^*)|. \tag{33}$$

Using a best fit value of m = 22.46, the temporal evolution of $\Phi^s(t)$ predicted by equation (33) agrees very well with $\Phi^s(t)$ directly calculated from SedFoam (see Figures 14a and 14c; IA = 0.996 and NRMSE = 5.3%). The resulting $\langle\Phi^s\rangle$ = 3.12 is also very close to that from SedFoam ($\langle\Phi^s\rangle$ = 3.37.). This best fit value of m is also similar to that used in the quasi-steady approach. It should be noted here that if we only consider the near-bed load component in SedFoam, the coefficient m was 13.04, which is close to that suggested for bedload by Ribberink (1998). Evidently, m is significantly increased (m = 22.46) due to the contribution from suspended sediment transport. If the phase shift is set to zero (φ = 0), the agreement is poor with IA = 0.970 and NRMSE = 41.8% (see Figure 14d). In summary, for modeling sediment transport driven by skewed wave motion in OWT without progressive wave streaming, the quasi-steady approach (e.g., Ribberink, 1998) works reasonably well, provided that the empirical coefficient m to be increased to account for suspended load transport.

When the same approach is applied to predict the time-dependent sediment transport rate of SedWaveFoam with progressive wave streaming, the agreement of the predicted wave-averaged sediment transport rate is poor. For example, when substituting the time-dependent bed shear stress of SedWaveFoam into equation (33), the predicted $\langle\Phi^s\rangle$ is 4.60, which is notably lower than the SedWaveFoam result ($\langle\Phi^s\rangle$ = 5.37). It is reminded that the time series of sediment transport rate presented in Figure 8e is more skewed during positive wave phase. We have discussed the concept of wave-stirring effect (see Figure 10) associated with nonlinear interaction of the streaming current and suspended sediment driven by more intense wave velocity. In the parameterization, the half wave-cycle concept (Dibajnia & Watanabe, 1998; Silva et al., 2006; Van der A et al., 2013) is first adopted to account for the stronger effect of wave-stirring during the positive wave phase. This approach acknowledges the distinct dominating mechanisms responsible for the transport and chooses to parameterize them with different empirical coefficients. Here $\Phi^s(t)$ is accounted separately for the positive (onshore) phase and negative (offshore) phase:

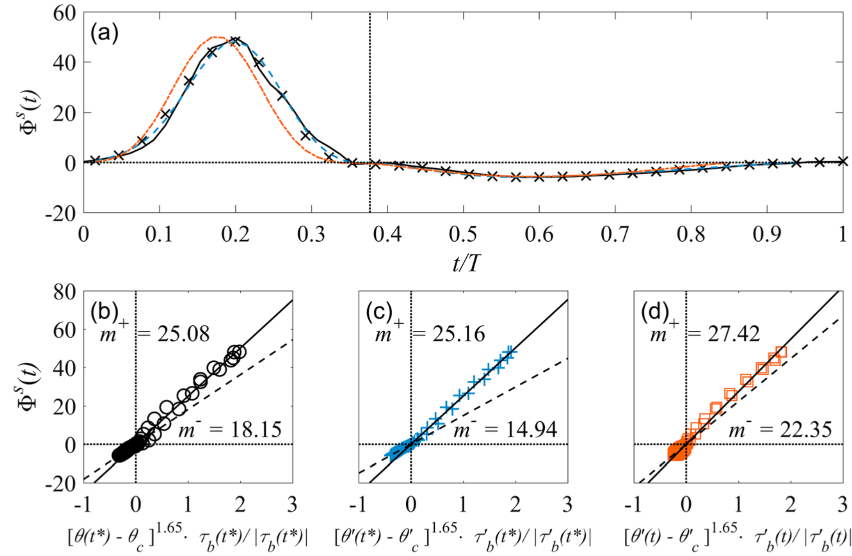

Figure 15. (a) Time series of $\Phi^s(t)$ computed by SedWaveFoam (crosses) is compared with those parameterized by to equation (34) with bed shear stress from SedWaveFoam with φ = 13.3° (black solid curve), and with bed shear stress from single-phase 1DV WBBL model with φ = 13.3° (blue dashed curve), and with bed shear stress from quasi-steady approach without the phase lag (red dashed-dot curve). (b–d) Agreement between $\Phi^s(t)$ of SedWaveFoam results versus these three parameterizations.

$$\Phi^{s+}(t) = m^+[\theta(t^*) - \theta_c]^n \;\; \tau_b(t^*)/|\tau_b(t^*)| \quad \text{where} \quad t < T^+$$
$$\Phi^{s-}(t) = m^-[\theta(t^*) - \theta_c]^n \;\; \tau_b(t^*)/|\tau_b(t^*)| \quad \text{where} \quad t \geq T^+, \tag{34}$$

in which T^+ is the duration of the wave crest and m^+ and m^- are the corresponding empirical coefficients for the positive phase and negative phase, respectively.

Using τ_b obtained from SedWaveFoam and equation (34) with best fit coefficients of m^+ = 25.08 and m^- = 18.15, very good agreement is obtained between the predicted $\Phi^s(t)$ and that directly calculated from SedWaveFoam results (*IA* = 0.998 and NRMSE = 3.9%, Figures 15a and 15b). The predicted wave-averaged sediment transport rate is $\langle\Phi^s\rangle$ = 5.35, which is very close to that from the SedWaveFoam simulation ($\langle\Phi^s\rangle$ = 5.37). From Figure 15b, we can also see two distinct slopes related to low and high sediment transport rates, which signify the effectiveness of different *m* values for positive and negative phases in this parameterization.

To test the complete parameterizations that include bed shear stress and sediment transport rate, we use $\theta'(t^*)$ from the single-phase 1DV WBBL model (phase lag of φ = 13.3° is included) or $\theta'(t)$ obtained from the quasi-steady approach (without phase lag) and added with $\langle\tau_{pws}\rangle$ using equation (23) to account for progressive wave streaming, and substituting the resulting nondimensional bed shear stress time series into equation (34) to estimate sediment transport rate. Using the $\theta'(t^*)$ from the single-phase 1DV WBBL model and equation (23) with best fit coefficients of m^+ = 25.16 and m^- = 14.94, the resulting time-dependent sediment transport rate agrees very well with SedWaveFoam results (*IA* = 0.999, NRMSE = 1.4%; see Figures 15a and 15c), and $\langle\Phi^s\rangle$ is overpredicted by only 0.3% ($\langle\Phi^s\rangle$ = 5.39). Similarly, using the $\theta'(t)$ obtained from the quasi-steady approach and equation (23) with best fit coefficients of m^+ = 27.42 and m^- = 22.35, the agreement on the predicted sediment transport rate is also good (*IA* = 0.988 and NRMSE = 20.9%; see Figures 15a and 15d) and $\langle\Phi^s\rangle$ is only underpredicted by 2.9% ($\langle\Phi^s\rangle$ = 5.22). We would like to point out that m^+ and m^- are determined solely based on best fit to minimize the errors. Hence, the fact that all cases shown in Figure 15 give significantly larger values of m^+ compared with m^- suggests that parameterizing wave-stirring effect associated with progressive wave streaming is necessary. Moreover, when we apply equation (34) to match the time series of sediment transport rate from the SedFoam result (OWT condition without progressive wave streaming), we obtain very similar values of m^+ = 22.59 and m^- = 21.16 (not shown), suggesting that wave-stirring effect discussed here is uniquely associated with progressive wave streaming. While

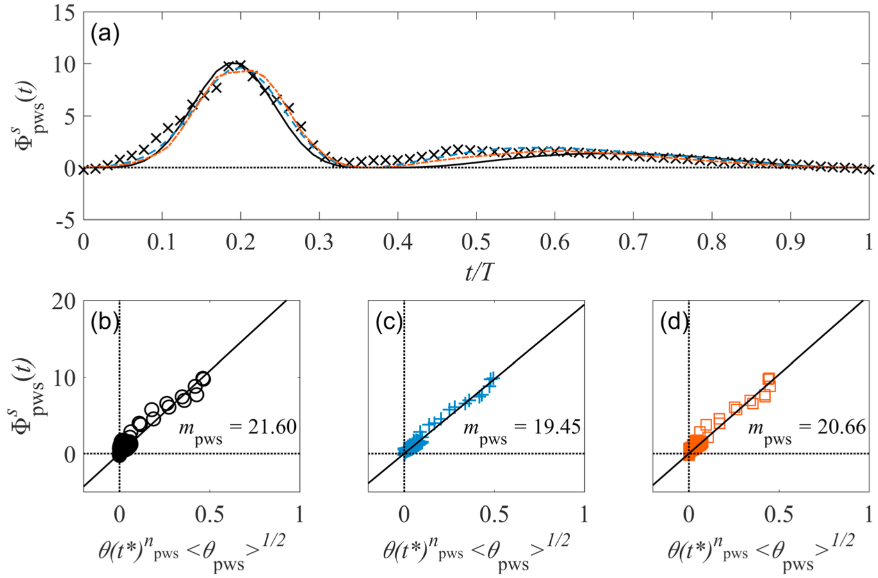

Figure 16. (a) Time series of $\Phi^s_{\text{pws}}(t)$ (crosses) compared to that parameterized by equation (35) with $\varphi = 0$ and time-dependent bed shear stress from quasi-steady approach (black solid curve), with $\varphi = 13.3°$ and time-dependent bed shear stress from single-phase 1DV WBBL (blue dashed curve), and with $\varphi = 13.3°$ and time-dependent bed shear stress from SedFoam (red dash-dotted curve). (b–d) Agreement between $\Phi^s_{\text{pws}}(t)$ from the SedWaveFoam results versus these parameterizations.

equation (34) is efficient, a functional relationship between m and intrawave (half wave period) velocity intensity needs to be established using extensive measured data and numerical simulations.

We would like to propose another method to parameterize the wave-stirring effect associated with progressive wave streaming in enhancing onshore sediment transport. In the present model study, we can compute the increase of Φ^s caused by the progressive wave streaming by subtracting the time-dependent sediment transport rate of SedFoam from that of SedWaveFoam, that is, $\Phi^s_{\text{pws}} = \Phi^s_{\text{SedWaveFoam}} - \Phi^s_{\text{SedFoam}}$. This time-dependent transport rate difference Φ^s_{pws} is associated with the difference in wave-averaged bed shear stress $\langle\tau_{\text{pws}}\rangle$ (estimated by equation (23)) normalized as $\langle\theta_{\text{pws}}\rangle$ and intrawave Shields parameter $\theta(t^*)$:

$$\Phi^s_{\text{pws}}(t) = m_{\text{pws}}\ \theta(t*)^{n_{\text{pws}}}\langle\theta_{\text{pws}}\rangle^{1/2}. \tag{35}$$

To relate the current strength caused by the progressive wave streaming, $\langle\theta_{\text{pws}}\rangle$ to the power of 0.5 is applied. The variable $\theta(t)$ (or $\theta(t^*)$) to a power of n_{pws} is included to parameterize suspended sediment due to (intra) wave-stirring effect. As discussed in section 3.3 (Figure 9), the progressive wave streaming mostly enhances the suspended load; hence, $n_{\text{pws}} = 2$ is adopted here. This is equivalent to the transport rate proportional to the intrawave velocity with a power of 4, and the entire equation (35) (with $\langle\theta_{\text{pws}}\rangle$ to a power of 1/2) is consistent with the suspended load parameterization of Bailard (1981) with a power of 5.

Using bed shear stress obtained from the quasi-steady formulation (equation (26)) with the phase lag $\varphi = 0$ in equation (35), the temporal evolution of $\Phi^s_{\text{pws}}(t)$ with a best fit $m_{\text{pws}} = 21.60$ agrees well with that from the numerical model (see Figures 16a and 16b; *IA* and NRMSE are 0.981 and 4.8%, respectively). The resulting net transport rate is 1.69, which is close to the numerical results of $\left\langle\Phi^s_{\text{pws}}\right\rangle = 2.00$. Similarly, substituting the bed shear stress calculated by the single-phase 1DV WBBL (with best fit $m_{\text{pws}} = 19.45$), and SedFoam (with best fit $m_{\text{pws}} = 20.66$) into equation (35) with $\varphi = 13.3°$, the agreement on temporal evolution of $\Phi^s_{\text{pws}}(t)$ is very good (see Figures 16a–16d) and the resulting net transport rates $\left\langle\Phi^s_{\text{pws}}\right\rangle$ are 1.95 and 1.69, reasonably close to the target value of 2.00. By explicitly including the intrawave wave-stirring effect in equation (35), only a single value of m_{pws} is needed for the entire wave period.

We would like to reiterate that the analysis presented above represents a first step toward integrating the mechanisms of enhanced onshore sediment transport due to progressive wave streaming by introducing the concept of wave-stirring transport based on two-phase flow numerical model results and experimental data of Dohmen-Janssen and Hanes (2002). For a complete parameterization and fully calibrated coefficients, SedWaveFoam and SedFoam models should be applied to many different wave conditions and other large wave flume data.

5. Conclusions

A free surface resolving Eulerian two-phase model, named SedWaveFoam, is successfully developed by merging SedFoam with InterFoam/waves2Foam in OpenFOAM frameworks to study the sediment transport under surface waves. The remarkable advantage of the new model is that the flow fields and sediment transport processes under surface waves in the entire water column are simultaneously resolved without the approximations typically adopted in boundary layer sediment transport models. Such an all-inclusive modeling approach has the potential to improve the understanding of wave-sediment interaction and prediction of the sediment transport rate under surface waves. The SedWaveFoam model is validated with the large wave flume data (Dohmen-Janssen & Hanes, 2002; Ribberink et al., 2000) of sheet flow under monochromatic nonbreaking surface waves. We focus on isolating and parameterizing the effect of free-surface on the resulting sediment transport processes.

The 1DV SedFoam simulation representing OWT condition is carried out, and the results are contrasted with SedWaveFoam results to examine the free surface effect on the sediment transport. In the SedWaveFoam results, the near-bed flow velocity and sediment flux are leaned to onshore direction due to the progressive wave streaming. The general magnitudes of WBBL thickness and sheet flow layer thickness are similar, but the free surface effect slightly enhances them. However, SedWaveFoam clearly produces more skewed and onshore-directed sediment transport rate particularly under the wave crest due to less offshore-directed current caused by the progressive wave streaming. As a result, the wave-averaged total sediment transport rate of SedWaveFoam is increased by about 1.6 times compared to that of SedFoam. Mainly, it is the intrawave-induced sediment flux that drives larger onshore sediment flux since it is enhanced when the flow is strong enough to suspend more sediment and to be further transported by the modulated mean current due to progressive wave streaming. The progressive wave streaming-induced wave-averaged bed shear stress, $\langle \tau_{\mathrm{pws}} \rangle$, is calculated as the difference in the wave-averaged bed shear stress between SedFoam and SedWaveFoam. The simple way to predict $\langle \tau_{\mathrm{pws}} \rangle$ (Nielsen, 2006; Nielsen & Callaghan, 2003; Van der A et al., 2013) seems to be reasonable with the bed roughness of $k_s = 2.5d_{50}$. It is notable that $\langle \tau_{\mathrm{pws}} \rangle$ is relatively small, and it contradicts the typical concept that $\langle \tau_{\mathrm{pws}} \rangle$ directly causes such significant increment of onshore-directed sediment transport rate.

Practical parameterizations are proposed using the model results to ultimately predict the wave-averaged total sediment transport rate with the available data. First, the several methods to predict the bed shear stress are compared. To better capture the phase lead of bed shear stress at the flow reversal, 1DV WBBL model and SedFoam are recommended as the alternative ways to approximate the bed shear stress under surface waves. Second, the linear relationship between sheet flow layer thickness and Shields parameter is found. Adopting a phase lag, the model results showed the capability of expanding the linear relationship to intrawave quantities to predict sheet flow layer thickness. Lastly, using Meyer-Peter and Mueller type power law bedload transport formula, a good agreement is obtained by considering the phase lag and suspended load in the power law for the OWT (SedFoam). However, when applied to predict sediment transport rate under surface waves, the empirical coefficient m in the power law formula should be separately estimated for each half wave-cycle to consider the wave-stirring effect associated with progressive wave streaming. An alternative intrawave approach to directly predict the wave-stirring effect throughout the entire wave cycle appears to be promising.

Finally, it should be pointed out that the knowledge gained in this study has been made possible by the utilization of a common numerical framework (OpenFOAM), which allows to isolate the contribution of free surface wave effects from two different modeling approaches, namely, SedFoam and SedWaveFoam.

Acknowledgments
This study is supported by NSF (OCE-1635151 and OCE-1356855) and Office of Naval Research (N00014-16-1-2853). Numerical simulations presented in this study were carried out using the Mills cluster at University of Delaware, and the SuperMic cluster at Louisiana State University via XSEDE (TG-OCE100015). Z. Cheng would like to thank the support of postdoctoral scholarship from Woods Hole Oceanographic Institution. We are grateful to the developers involved in OpenFOAM, who are the foundation of the model presented in this paper. The source code of SedWaveFoam and the case setup to reproduce the same results are publicly available via Community Surface Dynamics Modeling System (CSDMS) model repository maintained by GitHub: https://github.com/sedwavefoam/sedwavefoam (source code) and https://github.com/sedwavefoam/Dohmen-Janssen-and-Hanes-2002 (case setup).

References

Amoudry, L., Hsu, T.-J., & Liu, P. L.-F. (2005). Schmidt number and nearbed boundary condition effects on a two-phase dilute sediment transport model. *Journal of Geophysical Research*, *110*, C09003. https://doi.org/10.1029/2004JC002798

Amoudry, L., Hsu, T. J., & Liu, P. L. F. (2008). Two-phase model for sand transport in sheet flow regime. *Journal of Geophysical Research*, *113*, C03011. https://doi.org/10.1029/2007JC004179

Amoudry, L. O., & Liu, P. L. F. (2010). Parameterization of near-bed processes under collinear wave and current flows from a two-phase sheet flow model. *Continental Shelf Research*, *30*(13), 1403–1416. https://doi.org/10.1016/j.csr.2010.04.009

Bagnold, R. A. (1954). Experiments on a gravity-free dispersion of large solid spheres in a Newtonian fluid under shear. *Proceedings of the Royal Society A: Mathematical, Physical and Engineering Sciences*, *225*(1160), 49–63. https://doi.org/10.1098/rspa.1954.0186

Bailard, J. A. (1981). An energetics total load sediment transport model for a plane sloping beach. *Journal of Geophysical Research*, *86*(C11), 10938. https://doi.org/10.1029/JC086iC11p10938

Balachandar, S., & Eaton, J. K. (2009). Turbulent dispersed multiphase flow. *Annual Review of Fluid Mechanics*, *42*(1), 111–133. https://doi.org/10.1146/annurev. fluid. 010908.165243

Berberović, E., van Hinsberg, N. P., Jakirlić, S., Roisman, I. V., & Tropea, C. (2009). Drop impact onto a liquid layer of finite thickness: Dynamics of the cavity evolution. *Physical Review E*, *79*(3), 36306. https://doi.org/10.1103/PhysRevE.79.036306

Briganti, R., Torres-Freyermuth, A., Baldock, T. E., Brocchini, M., Dodd, N., Hsu, T.–. J., et al. (2016). Advances in numerical modelling of swash zone dynamics. *Coastal Engineering*, *115*, 26–41. https://doi.org/10.1016/j.coastaleng.2016.05.001

Carnahan, N. F., & Starling, K. E. (1969). Equation of state for nonattracting rigid spheres. *The Journal of Chemical Physics*, *51*(2), 635–636. https://doi.org/10.1063/1.1672048

Carstens, M. R., Nielson, F. M., & Altinbilek, H. D. (1969). Bedforms generated in the laboratory under an oscillatory flow. *CERC Tech. Memorandum 28*. U.S. Army Corps of Eng.

Chauchat, J., Cheng, Z., Nagel, T., Bonamy, C., & Hsu, T.-J. (2017). Sedfoam- 2.0: A 3-D two-phase flow numerical model for sediment transport. *Geoscientific Model Development*, *10*(12), 4367–4392. https://doi.org/10.5194/gmd-10-4367-2017

Chen, C. P., & Wood, P. E. (1985). A turbulence closure model for dilute gas-particle flows. *The Canadian Journal of Chemical Engineering*, *63*(3), 349–360. https://doi.org/10.1002/cjce.5450630301

Cheng, Z., Hsu, T.-J., & Calantoni, J. (2017). SedFoam: A multi-dimensional Eulerian two-phase model for sediment transport and its application to momentary bed failure. *Coastal Engineering*. https://doi.org/10.1016/j.coastaleng.2016.08.007

Danon, H., Wolfshtein, M., & Hetsroni, G. (1977). Numerical calculations of two-phase turbulent round jet. *International Journal of Multiphase Flow*, *3*(3), 223–234. https://doi.org/10.1016/0301-9322(77)90002-7

Dibajnia, M., & Watanabe, A. (1998). Transport rate under irregular sheet flow conditions. *Coastal Engineering*, *35*(3), 167–183. https://doi.org/10.1016/S0378-3839(98)00034-9

Ding, J., & Gidaspow, D. (1990). A bubbling fluidization model using kinetic theory of granular flow. *AICHE Journal*, *36*(4), 523–538. https://doi.org/10.1002/aic.690360404

Dohmen-Janssen, C. M., & Hanes, D. M. (2002). Sheet flow dynamics under monochromatic nonbreaking waves. *Journal of Geophysical Research*, *107*(C10), 3149. https://doi.org/10.1029/2001JC001045

Dohmen-Janssen, C. M., & Hanes, D. M. (2005). Sheet flow and suspended sediment due to wave groups in a large wave flume. *Continental Shelf Research*, *25*(3), 333–347. https://doi.org/10.1016/J.CSR.2004.10.009

Dohmen-Janssen, C. M., Hassan, W. N., & Ribberink, J. S. (2001). Mobile-bed effects in oscillatory sheet flow. *Journal of Geophysical Research*, *106*(C11), 27,103–27,115. https://doi.org/10.1029/2000JC000513

Dohmen-Janssen, C. M., Kroekenstoel, D. F., Hassan, W. N., & Ribberink, J. S. (2002). Phase lags in oscillatory sheet flow: Experiments and bed load modelling. *Coastal Engineering*, *46*(1), 61–87. https://doi.org/10.1016/S0378-3839(02)00056-X

Dong, P., & Zhang, K. (1999). Two-phase flow modelling of sediment motions in oscillatory sheet flow. *Coastal Engineering*, *36*(2), 87–109. https://doi.org/10.1016/S0378-3839(98)00052-0

Drake, T. G., & Calantoni, J. (2001). Discrete particle model for sheet flow sediment transport in the nearshore. *Journal of Geophysical Research*, *106*(C9), 19,859–19,868. https://doi.org/10.1029/2000JC000611

Drew, D. A. (1983). Mathematical modeling of two-phase flow. *Annual Review of Fluid Mechanics*, *15*, 261–291. https://doi.org/10.1146/annurev.fl.15.010183.001401

Fredsøe, J., Sumer, B. M., Kozakiewicz, A., Chua, L. H. C., & Deigaard, R. (2003). Effect of externally generated turbulence on wave boundary layer. *Coastal Engineering*, *49*(3), 155–183. https://doi.org/10.1016/S0378-3839(03)00032-2

Gidaspow, D. (1994). *Multiphase flow and fluidization—Continuum and kinetic theory descriptions*. New York: Academic, Press.

Gonzalez-Rodriguez, D., & Madsen, O. S. (2007). Seabed shear stress and bedload transport due to asymmetric and skewed waves. *Coastal Engineering*, *54*(12), 914–929. https://doi.org/10.1016/j.coastaleng.2007.06.004

Hassan, W. N. M., & Ribberink, J. S. (2010). Modelling of sand transport under wave-generated sheet flows with a RANS diffusion model. *Coastal Engineering*, *57*(1), 19–29. https://doi.org/10.1016/J.COASTALENG.2009.08.009

Henderson, S. M., Allen, J. S., & Newberger, P. A. (2004). Nearshore sandbar migration predicted by an eddy-diffusive boundary layer model. *Journal of Geophysical Research*, *109*, C06024. https://doi.org/10.1029/2003JC002137

Hirt, C. W., & Nichols, B. D. (1981). Volume of fluid (VOF) method for the dynamics of free boundaries. *Journal of Computational Physics*, *39*(1), 201–225. https://doi.org/10.1016/0021-9991(81)90145-5

Holmedal, L. E., Myrhaug, D., & Rue, H. (2003). The sea bed boundary layer under random waves plus current. *Continental Shelf Research*, *23*(7), 717–750. https://doi.org/10.1016/S0278-4343(03)00020-7

Hsu, T.-J., & Hanes, D. M. (2004). Effects of wave shape on sheet flow sediment transport. *Journal of Geophysical Research*, *109*, C05025. https://doi.org/10.1029/2003JC002075

Hsu, T.-J., Jenkins, J. T., & Liu, P. L.-F. (2004). On two-phase sediment transport: Sheet flow of massive particles. *Proceedings of the Royal Society A: Mathematical, Physical and Engineering Sciences*, *460*(2048), 2223–2250. https://doi.org/10.1098/rspa.2003.1273

Jackson, A. (2012). *A comprehensive tour of snappyHexMesh*. Darmstadt: 7th OpenFOAM Workshop.

Jacobsen, N. G., Fredsoe, J., & Jensen, J. H. (2014). Formation and development of a breaker bar under regular waves. Part 1: Model description and hydrodynamics. *Coastal Engineering*, *88*, 182–193. https://doi.org/10.1016/j.coastaleng. 2013.12.008

Jacobsen, N. G., Fuhrman, D. R., & Fredsøe, J. (2012). A wave generation toolbox for the open-source CFD library: OpenFoam®. *International Journal for Numerical Methods in Fluids*, *70*(9), 1073–1088. https://doi.org/10.1002/fld.2726

Jasak, H. (1996). Error analysis and estimation for finite volume method with applications to fluid flow, (PhD thesis). Imperial College, London, UK.

Jenkins, J. T., & Savage, S. B. (1983). A theory for the rapid flow of identical, smooth, nearly elastic, spherical particles. *Journal of Fluid Mechanics*, *130*(1), 187–202. https://doi.org/10.1017/S0022112083001044

Jensen, B. L., Sumer, B. M., & Fredsoe, J. (1989). Turbulent oscillatory boundary layers at high Reynolds numbers. *Journal of Fluid Mechanics*, *206*(1), 265–297. https://doi.org/10.1017/S0022112089002302

Johnson, P. C., & Jackson, R. (1987). Frictional–collisional constitutive relations for granular materials, with application to plane shearing. *Journal of Fluid Mechanics*, *176*(1), 67. https://doi.org/10.1017/S0022112087000570

Kim, Y., Zhou, Z., Hsu, T.-J., & Puleo, J. A. (2017). Large eddy simulation of dam-break-driven swash on a rough-planar beach. *Journal of Geophysical Research, Oceans*, *122*, 1274–1296. https://doi.org/10.1002/2016JC012366

Klostermann, J., Schaake, K., & Schwarze, R. (2013). Numerical simulation of a single rising bubble by VOF with surface compression. *International Journal for Numerical Methods in Fluids*, *71*(8), 960–982. https://doi.org/10.1002/fld.3692

Kranenburg, W. M., Hsu, T.-J., & Ribberink, J. S. (2014). Two-phase modeling of sheet-flow beneath waves and its dependence on grain size and streaming. *Advances in Water Resources*, *72*, 57–70. https://doi.org/10.1016/j.advwatres.2014.05.008

Kranenburg, W. M., Ribberink, J. S., Schretlen, J. J. L. M., & Uittenbogaard, R. E. (2013). Sand transport beneath waves: The role of progressive wave streaming and other free surface effects. *Journal of Geophysical Research: Earth Surface*, *118*, 122–139. https://doi.org/10.1029/2012JF002427

Kranenburg, W. M., Ribberink, J. S., Uittenbogaard, R. E., & Hulscher, S. J. M. H. (2012). Net currents in the wave bottom boundary layer: On waveshape streaming and progressive wave streaming. *Journal of Geophysical Research*, *117*, F03005. https://doi.org/10.1029/2011JF002070

Li, M., Pan, S., & O'Connor, B. A. (2008). A two-phase numerical model for sediment transport prediction under oscillatory sheet flows. *Coastal Engineering*, *55*(12), 1159–1173. https://doi.org/10.1016/j.coastaleng.2008.05.003

Longuet-Higgins, M. S. (1953). Mass transport in water waves. *Philosophical Transactions of the Royal Society of London A: Mathematical, Physical and Engineering Sciences*, *245*(903), 535–581. https://doi.org/10.1098/rsta.1953.0006

Longuet-Higgins, M. S. (2005). On wave set-up in shoaling water with a rough sea bed. *Journal of Fluid Mechanics*, *527*, 217–234. https://doi.org/10.1017/S0022112004003222

Mieras, R. S., Puleo, J. A., Anderson, D., Cox, D. T., & Hsu, T.-J. (2017). Large-scale experimental observations of sheet flow on a sandbar under skewed-asymmetric waves. *Journal of Geophysical Research: Oceans*, *122*, 5022–5045. https://doi.org/10.1002/2016JC012438

Nielsen, P. (1992). *Coastal bottom boundary layers and sediment transport*. World Scientific. https://doi.org/10.1142/1269

Nielsen, P. (2002). Shear stress and sediment transport calculations for swash zone modelling. *Coastal Engineering*, *45*(1), 53–60. https://doi.org/10.1016/S0378-3839(01)00036-9

Nielsen, P. (2006). Sheet flow sediment transport under waves with acceleration skewness and boundary layer streaming. *Coastal Engineering*, *53*(9), 749–758. https://doi.org/10.1016/j.coastaleng.2006.03.006

Nielsen, P., & Callaghan, D. P. (2003). Shear stress and sediment transport calculations for sheet flow under waves. *Coastal Engineering*, *47*(3), 347–354. https://doi.org/10.1016/S0378-3839(02)00141-2

O'Donoghue, T., & Wright, S. (2004a). Concentrations in oscillatory sheet flow for well sorted and graded sands. *Coastal Engineering*. https://doi.org/10.1016/j.coastaleng.2003.09.004

O'Donoghue, T., & Wright, S. (2004b). Flow tunnel measurements of velocities and sand flux in oscillatory sheet flow for well-sorted and graded sands. *Coastal Engineering*, *51*(11–12), 1163–1184. https://doi.org/10.1016/j.coastaleng.2004.08.001

Passalacqua, A., & Fox, R. O. (2012). Simulation of mono- and bidisperse gas-particle flow in a riser with a third-order quadrature-based moment method. *Industrial & Engineering Chemistry Research*, 120913145050004. https://doi.org/10.1021/ie300424m

Ribberink, J. S. (1998). Bed-load transport for steady flows and unsteady oscillatory flows. *Coastal Engineering*, *34*(1–2), 59–82. https://doi.org/10.1016/S0378-3839(98)00013-1

Ribberink, J. S., & Al-Salem, A. A. (1994). Sediment transport in oscillatory boundary layers in cases of rippled beds and sheet flow. *Journal of Geophysical Research*, *99*(C6), 12707. https://doi.org/10.1029/94JC00380

Ribberink, J. S., Dohmen-Janssen, C. M., Hanes, D. M., McLean S. R., & Vincent C. E. (2000). Near-bed sand transport mechanisms under waves: A large-scale flume experiment (SISTEX99). In *Proceedings 27th International Conference on Coastal Engineering* (pp. 3263–3276). Sydney.

Ribberink, J. S., van der Werf, J. J., O'Donoghue, T., & Hassan, W. N. M. (2008). Sand motion induced by oscillatory flows: Sheet flow and vortex ripples. *Journal of Turbulence*, *9*, N20. https://doi.org/10.1080/14685240802220009

Rodi, W. (1993). *Turbulence models and their application in hydraulics*. CRC Press.

Ruessink, B. G., van den Berg, T. J. J., & van Rijn, L. C. (2009). Modeling sediment transport beneath skewed asymmetric waves above a plane bed. *Journal of Geophysical Research*, *114*, C11021. https://doi.org/10.1029/2009JC005416

Rusche, H. (2002). Computational fluid dynamics of dispersed two-phase flows at high phase fractions, (PhD thesis). Imperial College of Science, London, UK.

Schaeffer, D. G. (1987). Instability in the evolution equations describing incompressible granular flow. *Journal of Differential Equations*, *66*(1), 19–50. https://doi.org/10.1016/0022-0396(87)90038-6

Schretlen, J. L. M. (2012). Sand transport under full-scale progressive surface waves, (PhD thesis). University of Twente, Enschede. Retrieved from https://research.utwente.nl/en/publications/sand-transport-under-full-scale-progressive-surface-waves

Silva, P. A., Temperville, A., & Seabra Santos, F. (2006). Sand transport under combined current and wave conditions: A semi-unsteady, practical model. *Coastal Engineering*, *53*(11), 897–913. https://doi.org/10.1016/j.coastaleng.2006.06.010

Soulsby, R. (1997). *Dynamics of marine sands: A manual for practical applications*. London, UK: Thomas Telford.

Srivastava, A., & Sundaresan, S. (2003). Analysis of a frictional-kinetic model for gas-particle flow. *Powder Technology*, *129*(1–3), 72–85. https://doi.org/10.1016/S0032-5910(02)00132-8

Sumer, B. M., Jensen, P. M., Sørensen, L. B., Fredsøe, J., Liu, P. L. F., & Carstensen, S. (2010). Coherent structures in wave boundary layers. Part 2. Solitary motion. *Journal of Fluid Mechanics*, *646*, 207–231. https://doi.org/10.1017/S0022112009992837

Sumer, B. M., Kozakiewicz, A., Fredsøe, J., & Deigaard, R. (1996). Velocity and concentration profiles in sheet-flow layer of movable bed. *Journal of Hydraulic Engineering*, *122*(10), 549–558. https://doi.org/10.1061/(ASCE)0733-9429(1996)122:10(549)

Sweby, P. K. (1984). High resolution schemes using flux limiters for hyperbolic conservation laws. *SIAM Journal on Numerical Analysis*, *21*(5), 995–1011. https://doi.org/10.1137/0721062

Trowbridge, J., & Madsen, O. S. (1984). Turbulent wave boundary layers: 2. Second-order theory and mass transport. *Journal of Geophysical Research*, *89*(C5), 7999. https://doi.org/10.1029/JC089iC05p07999

Van der A, D. A., Ribberink, J. S., Van der Werf, J. J., O'Donoghue, T., Buijsrogge, R. H., & Kranenburg, W. M. (2013). Practical sand transport formula for non-breaking waves and currents. *Coastal Engineering*, *76*, 26–42. https://doi.org/10.1016/j.coastaleng.2013.01.007

Van Rijn, L. C. (1987). Mathematical modelling of morphological processes in the case of suspended sediment transport. *Delft Hydra*. Communication, (382). Retrieved from https://repository.tudelft.nl/islandora/object/uuid:c1c1fce6-afc6-4ca3-b707-e108f256048c/datastream/OBJ

Van Rijn, L. C. (1993). *Principles of sediment transport in rivers, estuaries and coastal seas* (Vol. 1006). Amsterdam: Aqua publications.

Watanabe, A., & Sato, S. (2005). A sheet-flow transport rate formula rate formula for asymmetric forward-leaning waves and currents. In *Proceedings 29th International Conference on Coastal Engineering* (pp. 1703–1714). World Scientific. https://doi.org/10.1142/9789812701916_0136

Willmott, C. J. (1981). On the validation of models. *Physical Geography*, *2*(2), 184–194. https://doi.org/10.1080/02723646.1981.10642213

Willmott, C. J., & Wicks, D. E. (1980). An empirical method for the spatial interpolation of monthly precipitation within California. *Physical Geography*, *1*(1), 59–73. https://doi.org/10.1080/02723646.1980.10642189

Wilson, K. C. (1987). Analysis of bed-load motion at high shear stress. *Journal of Hydraulic Engineering*, *113*(1), 97–103. https://doi.org/10.1061/(ASCE)0733-9429(1987)113:1(97)

Yu, X., Hsu, T.-J., & Hanes, D. M. (2010). Sediment transport under wave groups: Relative importance between nonlinear waveshape and nonlinear boundary layer streaming. *Journal of Geophysical Research*, *115*, C02013. https://doi.org/10.1029/2009JC005348

Zhang, Y., Chen, Y., Gullman-Strand, J., Dao, M., Jaiman, R. K., & Zhang, W. (2015). Numerical simulation of current generation in deep water basin. A*SME. Int. Conf. Off. Mech. Arctic Eng*., Vol. 2: CFD and VIV ():V002T08A014. https://doi.org/10.1115/OMAE2015-41812

Zhou, Z., Hsu, T.-J., Cox, D., & Liu, X. (2017). Large-eddy simulation of wave-breaking induced turbulent coherent structures and suspended sediment transport on a barred beach. *Journal of Geophysical Research: Oceans*, *122*, 207–235. https://doi.org/10.1002/2016JC011884